

 Open access • Journal Article • DOI:10.1007/S00410-018-1544-4

Geochemical and petrological diversity of mafic magmas from Mount St. Helens

— [Source link](#) 

Maren Wanke, Michael A. Clynne, Albrecht von Quadt, Torsten Vennemann ...+1 more authors

Institutions: ETH Zurich, United States Geological Survey, University of Lausanne

Published on: 03 Jan 2019 - Contributions to Mineralogy and Petrology (Springer Berlin Heidelberg)

Topics: Basaltic andesite, Basalt, Mafic, Andesite and Flux melting

Related papers:

- [Geochemistry, petrogenesis, and tectonic implications of central High Cascade mafic platform lavas](#)
- [Petrogenesis of Mount St. Helens dacitic magmas](#)
- [Origin of rhyolite and rhyodacite lavas and associated mafic inclusions of Cape Akrotiri, Santorini: the role of wet basalt in generating calcalkaline silicic magmas](#)
- [The petrology and geochemistry of the Ocate volcanic field, north-central New Mexico](#)
- [Origin of andesite and its bearing on the Island arc structure](#)

Share this paper:    

View more about this paper here: <https://typeset.io/papers/geochemical-and-petrological-diversity-of-mafic-magmas-from-vw3qnp35ss>

Geochemical and petrological diversity of mafic magmas from Mount St. Helens

Journal Article**Author(s):**

Wanke, Maren; Clynne, Michael A.; von Quadt, Albrecht; Vennemann, Torsten W.; Bachmann, Olivier

Publication date:

2019-01

Permanent link:

<https://doi.org/10.3929/ethz-b-000315288>

Rights / license:

[In Copyright - Non-Commercial Use Permitted](#)

Originally published in:

Contributions to Mineralogy and Petrology 174, <https://doi.org/10.1007/s00410-018-1544-4>

Funding acknowledgement:

146268 - Towards a quantitative understanding of caldera-forming events (SNF)

1 Geochemical and petrological diversity of mafic magmas from 2 Mount St. Helens

3 Maren Wanke^{1*}, Michael A. Clynne², Albrecht von Quadt¹, Torsten W. Vennemann³, Olivier
4 Bachmann¹

5 ¹Institute of Geochemistry and Petrology, Department of Earth Sciences, ETH Zürich,
6 Clausiusstrasse 25, 8092 Zürich, Switzerland

7 *maren.wanke@erdw.ethz.ch

8 ²U.S. Geological Survey, Volcano Science Center, Menlo Park, CA 94025, USA

9 ³Institut des Dynamiques de la Surface Terrestre, Université de Lausanne, CH-1015 Lausanne,
10 Switzerland

11 **Abstract**

12 Quaternary eruptive products in the Cascade arc include a variety of different basalt types.
13 At Mount St. Helens (MSH), the most active volcano in the Cascades throughout the last
14 35 ka, three different mafic endmembers erupted at the end of the Castle Creek period
15 (1900-1700 years B.P.): (1) high-field strength element (HFSE)-rich basalt enriched in K,
16 Ti, P, and incompatible trace elements, (2) low-K olivine tholeiite (LKOT) with lower
17 amounts of incompatible trace elements, and (3) calc-alkaline (arc-type) basaltic andesite
18 with a typical subduction signature, i.e., enrichment in fluid-mobile large ion lithophile
19 elements (LILE) relative to immobile high field strength elements (HFSE). Each type has
20 compositions projecting backwards to more primitive endmembers in the Cascades. Single
21 units encompassing basaltic to basaltic andesitic compositions with intermediate trace
22 element abundances form two almost continuous trends towards basaltic andesite. These
23 trends are interpreted to result from assimilation of pre-existing, more evolved, calc-
24 alkaline material (and in one case mixing of different mafic magma types) during
25 migration of the magmas through the crust. Most of the erupted basalts are porphyritic (10-
26 30 %) with an assemblage dominated by olivine and plagioclase and show disequilibrium
27 textures preventing detailed reconstruction of mantle melting processes. Although typical
28 hydrous arc basalt produced by flux melting in the mantle is absent in the eruptive
29 products of MSH, arc-type basaltic andesite suggests its presence at depth. LKOT magmas
30 are interpreted as decompression melts from the upper mantle, whereas HFSE-rich basalts

31 are likely derived from the water-poor periphery of the main flux melting regime,
32 potentially tapping a trace element enriched source. Primitive spinel compositions and
33 whole-rock trace element variations indicate at least two distinct, relatively fertile
34 lherzolite sources for these two basalt types. Weak crustal zones associated with an old
35 fracture system beneath MSH likely provide conduits for fast and isolated ascent of
36 distinct batches of magma, bypassing the lower crustal mush zone. The eruption of the
37 basalts through the upper crustal magma system and main edifice is consistent with an
38 offset plumbing system suggested by geophysical data.

39 **Introduction**

40 Primitive basalts at convergent margins provide valuable insights into magma generation
41 beneath volcanic arcs. The North American Cascades are well known for their variety of
42 primitive magmas. Earlier studies of mafic magmas in the Cascades have established three
43 compositional endmembers: (1) high-field strength element (HFSE-rich) basalts, also
44 referred to as ocean-island basalts (OIB) or intraplate basalts (IPB), (2) low-K, high-Al
45 olivine tholeiites (LKOT, HAOT), and (3) calc-alkaline arc basalts (CAB) and basaltic
46 andesites (BA) (Bacon 1990; Leeman et al. 1990; Bacon et al. 1997; Borg et al. 1997;
47 Clynne and Borg 1997; Conrey et al. 1997; Reiners et al. 2000; Grove et al. 2002; Leeman
48 et al. 2005; Smith and Leeman 2005; Hildreth 2007; Schmidt et al. 2008; Rowe et al. 2009;
49 Moore and DeBari 2012; Sisson et al. 2014; Mullen et al. 2017). Minor variants include
50 ultrapotassic shoshonites and absarokites (Bacon 1990; Conrey et al. 1997; Schmidt et al.
51 2008) as well as high-Mg andesites (Baker et al. 1994; Bacon et al. 1997; Clynne and Borg
52 1997; Grove et al. 2002; Sas et al. 2017; Streck and Leeman 2018). To avoid any
53 interpretative association with a certain tectonic setting, we use the term *HFSE-rich*
54 *basalts* (Schmidt et al. 2008) for basalts that lack or have small depletions of HFSE, high
55 Nb concentrations, high light to heavy rare earth element ratios (LREE/HREE) similar to
56 OIB, and overall enriched concentrations in incompatible trace elements relative to mid
57 ocean ridge basalts (MORB). LKOTs have variable compositions throughout the arc, but
58 are comparable to enriched (E)-MORB, although with higher Al₂O₃ contents (>17 %) and
59 slightly enriched incompatible trace element abundances, albeit distinctly lower than in
60 HFSE-rich basalts. CAB and BA compositions vary along-arc, but are commonly enriched
61 in fluid-mobile large ion lithophile elements (LILE) and LREE relative to immobile HFSE

1
2
3
4
5
6
7
8
9
10
11
12
13
14
15
16
17
18
19
20
21
22
23
24
25
26
27
28
29
30
31
32
33
34
62 and HREE, associated with a hydrous slab-derived component. The diversity among
63 primitive basalts has been assigned to the existence of at least three mantle components
64 that are irregularly distributed beneath the arc: (1) a source enriched in incompatible
65 elements relative to MORB (similar to that producing OIB), (2) depleted sub-arc mantle
66 similar to that producing MORB, but weakly modified by a subduction component
67 (HAOT-/LKOT-type mantle), and (3) a modern slab-derived subduction component and/or
68 mantle source metasomatized by ancient subduction-related fluids.

69 Mafic magmas are most abundant from southern Washington to Northern California, but
70 all basalt types occur widely distributed along and across the arc (Hildreth 2007). Primitive
71 magmas in the Cascades typically erupt from monogenetic and shield vents, but also erupt
72 near stratovolcanoes that are dominated by andesite and/or dacite. When associated with
73 stratovolcanoes, basalts preferentially erupt from the periphery of these systems and/or
74 become more primitive with distance from the central vents. Examples include Mt. Baker
75 (Moore and DeBari 2012), Mt. Rainier (Fiske et al. 1963; Sisson et al. 2014), Mt. Adams
76 (Hildreth and Fierstein 1997), and Mt. Hood (Scott et al. 1997). Mount St. Helens (MSH)
77 forms an exception with respect to basaltic vent localities. Different basalt types erupted
78 through the axial system of the volcano, from vents on the southern and northern to
79 northwestern flanks, less than 1-2 km from the main crater.

80 Descriptions of quaternary basaltic magmas in the MSH area can be found in Smith
81 (1984), Leeman et al. (1990), Smith et al. (1993), Smith and Leeman (2005) and Leeman
82 and Smith (2018). They defined three types of mafic magmas at MSH including (1) calc-
83 alkaline olivine + plagioclase \pm clinopyroxene basalt enriched in K₂O, TiO₂, and
84 incompatible trace elements, also referred to as *north flank basalt* that is equivalent to our
85 *HFSE-rich basalt*, (2) transitional olivine + plagioclase basalt with low K₂O and
86 incompatible trace element abundances transitional between calc-alkaline and tholeiitic
87 basalts, the so-called *Cave Basalt* on the south flank of the volcano that we refer to as
88 *LKOT*, and (3) olivine + plagioclase basaltic andesite with incompatible trace element
89 compositions intermediate between the two basalt types that represent mixtures of basaltic
90 endmembers and variable amounts of more evolved calc-alkaline material (Leeman et al.
91 2005; Smith and Leeman 2005; Leeman and Smith 2018). These studies attributed the

1
2
3
4
5
6
7
8
9
10
11
12
13
14
15
16
17
18
19
20
21
22
23
24
25
26
27
28
29
30
31
32
33
34
35
36
37
38
39
40
41
42
43
44
45
46
47
48
49
50
51
52
53
54
55
56
57
58
59
60
61
62
63
64
65

92 compositional diversity in mafic magmas to different degrees of relatively dry melting of a
93 heterogeneous mantle.

94 Although previous studies address the petrogenesis of some mafic magmas at MSH, new
95 geologic mapping, geochronologic data (Clynne et al. 2008), and accompanying chemical
96 data revealed a refined stratigraphy with at least eight basaltic and basaltic andesitic units
97 (summarized in Pallister et al. 2017). Combined with recent geophysical imaging (Hansen
98 et al. 2016; Kiser et al. 2016; Kiser et al. 2018) these new data provide the background for
99 a more detailed investigation of mafic magmas at MSH.

100 This study presents new major and trace element compositions for 45 samples erupted
101 during the Castle Creek period, including Sr-, Nd- and O-isotopes for 12 samples and
102 mineralogic data for 6 mafic units. Furthermore, a data compilation of Castle Creek rocks
103 with whole-rock compositions from the literature and 287 previously unpublished samples,
104 mostly obtained during mapping of the volcano by E. Wolfe and M. Clynne, are presented.
105 These reveal remarkable geochemical trends and compositional endmembers, partly
106 differing from those defined by Smith and Leeman (1993) and Leeman and Smith (2018).
107 Using the extended dataset and petrologic data, the aims are to (1) specify the
108 characterization of different mafic endmembers at MSH, (2) evaluate pre-existing
109 hypotheses concerning their origin, and (3) focus on the implications of the observed
110 chemical and petrological variability for the MSH magmatic system, particularly
111 considering the close spatial and temporal eruption of different basalt types, andesites, and
112 dacites.

113 **Geologic setting**

114 MSH is a dominantly dacitic stratovolcano that lies about 50 km west of the main volcanic
115 axis in the southern Washington Cascades. The area belongs to the Columbia segment of
116 the arc (Schmidt et al. 2008), where the Juan de Fuca plate is subducted beneath North
117 America. The oblique subduction induces dextral shear between the two plates and results
118 in clock-wise rotation of large crustal blocks, such as the Oregon forearc block, that leads
119 to northward translation of the forearc and intra-arc extension (Wells et al. 1998; Hildreth
120 2007). MSH is located in a small tensional pull-apart basin formed by a dextral offset in
121 the N-NW-trending right-lateral strike-slip fault system known as the St. Helens seismic

122 zone (SHSZ) that intersects with a NE-trending set of pre-Quaternary fractures (Fig. 1)
123 (Weaver et al. 1987). The SHSZ coincides with the eastern boundary of the oceanic
124 Siletzia terrane (Parsons et al. 1999) that was accreted to North America in the early
125 Eocene (Wells et al. 2014) and with the western boundary of the Spirit Lake batholith
126 (Bedrosian et al. 2018). Recent geophysical imaging revealed two low velocity zones
127 interpreted as magma storage zones in the upper and lower crust beneath MSH (Kiser et al.
128 2016). The lower crustal velocity anomaly appears to be shifted about 10-20 km southeast
129 of the volcano and extends from about 20 km depth to the Moho at 40 km.

130 **Eruptive history**

131 The modern edifice of MSH developed over the last 4 ka, but volcanism in the MSH area
132 dates back to at least 270 ka (Clynne et al. 2008), and Claiborne et al. (2010) reported
133 sparse zircons as old as 500-600 ka in some of the dacites. The stratigraphy of pyroclastic
134 deposits of the volcano has been well established by Crandell and Mullineaux in the
135 1960s-1980s (Crandell 1987; Mullineaux 1996). It was recently refined by new geological
136 mapping aided by argon and radiocarbon geochronology, and paleomagnetic directional
137 data (Clynne et al. 2008 and Appendix A1). The eruptive history of MSH has been divided
138 into four eruptive stages separated by repose intervals of several thousand years. The
139 youngest stage, Spirit Lake, has been further subdivided into seven eruptive periods
140 separated by dormant intervals of several hundred years: Smith Creek (3.9-3.3 ka), Pine
141 Creek (3.0-2.55 ka), Castle Creek (2.025-1.7 ka), Sugar Bowl (1.05 ka), Kalama (1479-
142 1725 CE), Goat Rocks (1800-1857 CE), and Modern (1980-present) eruptive periods.

143 The Castle Creek eruptive period was the most compositionally diverse period in the
144 volcano's history and the only one that erupted basalts. Compositions from dacite to basalt
145 were erupted between ~2025 and 1700 years B.P. in three phases (Table 1) (Pallister et al.
146 2017). The early phase (~2025-1990 years B.P.) primarily encompassed dacitic eruptions
147 of lava domes, pyroclastic flows and lahars, tephra Bi and several silicic andesitic to
148 dacitic lava flows. Deposits of the middle Castle Creek phase are confined to the southern
149 flank of the volcano. They include three compositionally different basalt units (erupted
150 around 1895 years B.P.). During the late Castle Creek phase (~1800-1700 years B.P.) a
151 number of basaltic to dacitic lavas and tephtras were emplaced on the northern and eastern

152 flanks of the volcano. The most prominent departures from the stratigraphy established by
153 Crandell and Mullineaux are the redefinition of some basaltic andesitic and andesitic
154 tephra (Bh, Bo) and lavas previously recognized as Castle Creek age to Pine Creek age
155 and the recognition that the basaltic tephra Bu consists of three eruptions (Bu1, Bu2, Bu3)
156 of different ages. This redefined the Castle Creek basalts on the southern flank to be older
157 than those on the northern flank.

158 **Analytical methods**

159 **Major and trace elements**

160 The abundances of major element oxides from 45 samples of the Castle Creek eruptive
161 period were analyzed by X-ray fluorescence analysis (XRF) using a PANalytical AXIOS
162 spectrometer at ETH Zürich. Trace elements were measured by laser ablation - inductively
163 coupled plasma source mass spectrometry (LA-ICPMS) on the fused glass beads used for
164 XRF analyses using a Geolas Laser Ablation System coupled with an Elan 6100 DRC
165 (Perkin Elmer) mass spectrometer. Samples, blanks and standards were ablated for 60 s
166 with 10 Hz and a beam diameter of 90 μm (except for a NIST 610 standard that was
167 ablated with a beam diameter of 40 μm). The data were processed using the data reduction
168 software SILLS (Guillong et al. 2008). All data and results for a BCR-2 standard and
169 duplicates analyzed along with the sample suite for major and trace elements are reported
170 in Appendix A2.

171 **Isotopes**

172 Strontium and neodymium isotope compositions of 12 samples were analyzed on 50 to 70
173 mg whole rock powder digested in HF and HNO₃. Sr and Nd were subsequently separated
174 by ion-exchange chromatography in columns with SrSpec, TRUSpec and LnSpec Eichrom
175 resins (Pin et al. 1994). Strontium was loaded onto outgassed Re single filaments with
176 HNO₃ and Ta emitter, whereas the Nd fraction was loaded onto double filaments with 2N
177 HCl. Both were analyzed with a Thermo Scientific TritonPlus mass spectrometer operated
178 in static mode at ETH Zürich. Repeated measurements of NBS 987 and JNd-i yielded an
179 $^{87}\text{Sr}/^{86}\text{Sr}$ mean ratio of 0.710234 ± 0.000004 and a $^{143}\text{Nd}/^{144}\text{Nd}$ mean ratio of
180 0.512100 ± 0.000003 , respectively.

181 Oxygen was extracted by CO₂ laser fluorination using about 50 mbars of F₂ as reagent at
182 the University of Lausanne. The CO₂ laser was pulsed at a rate of 50 Hz with a duration of
183 20 ms, and the beam size was successively lowered from 1850 to 260 μm. Oxygen was
184 cleaned from residual F₂ by passing the gas over heated KCl and adsorbing the oxygen on
185 a molecular sieve (13X) prior to expanding it into the dual inlet of a Thermo Finnigan
186 MAT 253 mass spectrometer. Oxygen isotope compositions are reported relative to
187 standard mean ocean water (VSMOW) in the common δ-notation in parts per thousand (‰,
188 permil). NBS-28 quartz standard (9.64 ‰) was used for reference and drift correction for
189 each run. The analyses were performed on 1.7-2.7 mg of whole-rock powder and 0.5-2.4
190 mg mineral separates, respectively. Duplicate analyses for different days reproduced to an
191 average precision of better than ±0.2 ‰. Sr, Nd, and O isotopic ratios are given in
192 Appendix A2.

193 **Mineral analyses**

194 Backscattered electron images of thin sections and mineral grain mounts were obtained
195 using a JEOL JSM-6390LA scanning electron microscope (SEM) at the ETH Zürich.
196 Analyses of major and some minor elements in minerals were performed on a JEOL JXA-
197 8200 electron probe micro analyzer (EPMA) at the ETH Zürich using five wavelength
198 dispersive spectrometers. Plagioclase was measured using 15 kV accelerating voltage, 10
199 nA beam current, and a spot size of 5 μm. Na and K were analyzed first. Olivine was
200 analyzed with 20 kV, 30 nA, and a focused beam, spinel with 15 kV, 30 nA, and a focused
201 beam. V and Mn were corrected for K_β peak overlaps of Ti and Cr. All mineral data and
202 details about calibration, standard analyses and errors are reported in Appendix A3.

203 **Geochemical characteristics**

204 **Major and trace elements**

205 Volcanic rocks erupted during the Castle Creek period from MSH encompass basaltic
206 through dacitic compositions, with a great heterogeneity at the mafic end of the spectrum.
207 Mafic rocks include basalts, trachybasalts, and basaltic andesites (Fig. 2a) (Le Bas et al.
208 1986). They have medium-K, subalkaline compositions, with exception of the highest-K
209 basalts that are alkaline (Fig. 2b) (Irvine and Baragar 1971; Gill 1981). High FeO/MgO

1 ratios classify the basalts as tholeiitic, whereas basaltic andesites to dacites are
2 predominantly calc-alkaline (Fig. 2c) (Miyashiro 1974).

3
4 212 Three groups of mafic magma are identified at MSH that each resemble more primitive
5
6 213 variants of the same type in the Cascades: (1) HFSE-rich basalts encompassing alkaline
7
8 214 and calc-alkaline high-K basalts (bsf/Bu1, bnf/Bu2, bcc/Bu3; unit names as in Table 1), (2)
9
10 215 LKOT formed by low-K basalts (bc, bpc), and (3) calc-alkaline or arc-type basaltic
11
12 216 andesites (mng, ass, mtt), which are relatively evolved, but represent the most mafic
13
14 217 variants of this rock type at MSH (Fig. 2, 3). The first two endmembers are equivalent to
15
16 218 basalts described by Smith and Leeman (1993) and Leeman and Smith (2018). We will
17
18 219 refer to third endmember as *arc-type* basaltic andesites to distinguish them from previously
19
20 220 described calc-alkalic basaltic andesites (as defined by Miyashiro 1974) that have lower
21
22 221 SiO₂ contents, but lack pronounced chemical arc signatures (i.e., enrichment in LILE and
23
24 222 LREE relative to HFSE and HREE). The most notable features of Castle Creek rocks are
25
26 223 the two distinct chemical trends from the HFSE-rich and LKOT-like basalt endmembers
27
28 224 that almost merge around 5-6 wt% MgO and 52-54 wt% SiO₂ (Fig. 2-4).

29 *HFSE-rich basalts*

30
31 226 The basalt of the north flank (bnf) and the associated tephra layer Bu2 form the
32
33 227 endmember of the HFSE-rich basalts. They are characterized by high abundances of K₂O,
34
35 228 Na₂O, TiO₂, and P₂O₅ (Fig. 3). Their compositions overlap with those of nepheline-
36
37 229 normative HFSE-rich basalts in the southern Washington Cascades (*ALK*, Leeman et al.
38
39 230 2005) (Fig. 3, 4). They have high incompatible trace element abundances closely
40
41 231 approaching those of OIB (Fig. 5). Their high LREE/HREE ratios (La/Yb = 8.6-12.9)
42
43 232 produce patterns roughly parallel to those of the Castle Creek dacites, but at higher total
44
45 233 abundances. None of the basalts at MSH has a pronounced Eu-anomaly (Eu/Eu* = 0.92-
46
47 234 1.08). HFSE-rich basalts are slightly enriched in LILE and HFSE over REE relative to
48
49 235 MORB (Ba/La = 13.7-14.8, Pb/Ce = 0.04-0.06) and have positive Nb-Ta-anomalies (Nb/La
50
51 236 = 1.3-1.5).

52
53 237 The basalt of Castle Creek (bcc) with the associated tephra layer Bu3 and the basalt of the
54
55 238 south flank (bsf) form nearly continuous chemical trends towards (low-SiO₂) basaltic
56
57 239 andesite. These more evolved units have lower abundances of incompatible trace elements

240 and show depletion in Nb and Ta with decreasing MgO ($Nb/La = 1.5-0.8$). Some of these
241 samples resemble more primitive hypersthene-normative HFSE-rich basalts in the southern
242 Washington Cascades (*OIB*, Leeman et al. 2005).

243 *LKOT*

244 The LKOT endmember is represented by the 0.25 km³ (Williams et al. 2004) Cave Basalt
245 (bc) lava flow on the southern flank of MSH. It has compositions closely approaching
246 those of primitive southern Washington LKOTs (Leeman et al. 2005), but with slightly
247 higher abundances of incompatible elements due to its more evolved nature ($MgO = 6.1-$
248 7.3 wt%). The Cave Basalt has distinctly lower abundances of K_2O , Na_2O , TiO_2 , and P_2O_5 ,
249 and higher abundances of CaO , FeO , and Al_2O_3 than HFSE-rich basalts. It also has lower
250 concentrations of most incompatible trace elements. Some elements (e.g., Ni, Cr, V, Y)
251 occur in the same abundance as in HFSE-rich basalts. Incompatible trace elements exceed
252 those of enriched (E)-MORB. They are slightly enriched in LREE over HREE ($La/Yb =$
253 $3.4-4.1$) and LILE relative to REE ($Ba/La = 13-15$, $Pb/Ce = 0.08-0.10$) (Fig. 5). Some Cave
254 Basalt samples have a weak negative Nb-Ta-anomaly ($Nb/La = 0.8-1.0$).

255 The pre-Cave basalt (bpc) that preceded the eruption of the Cave Basalt forms a
256 compositional trend from this LKOT endmember towards basaltic andesite (Fig. 2). On
257 compositional variation diagrams against MgO, the pre-Cave Basalt forms a higher-K to
258 lower-K trend that merges at basaltic andesitic compositions, but at higher TiO_2 and CaO
259 contents than basaltic andesites of the HFSE-rich basalt group (Fig. 3). Incompatible trace
260 elements exceed those of the Cave Basalt.

261 *Arc-type basaltic andesites*

262 Previously undescribed arc-type basaltic andesites include the basaltic andesite of Nelson
263 Glacier (mng), the basaltic andesite of Truman Trail (mtt) and the andesite of Sasquatch
264 Steps (asa). Despite some variability among these units, the basaltic andesite of Nelson
265 Glacier is used to represent this group as it shows the least disequilibrium textures
266 (Appendix A5). Primitive CAB did not erupt from MSH, thus, the basaltic andesite of
267 Nelson Glacier represents the most mafic endmember of this magma type. Its compositions
268 plot close to the converging point of the LKOT and HFSE-rich basalt groups, but at higher
269 Al_2O_3 and lower TiO_2 , FeO , and P_2O_5 , similar to Cascade CAB (Fig. 3). Arc-type basaltic

270 andesites have steep REE patterns ($\text{La/Yb} = 6.4\text{-}9.2$) and show distinct enrichment in fluid-
271 mobile LILE, U and Pb ($\text{Ba/La} = 19.2\text{-}23.0$, $\text{Pb/Ce} = 0.12\text{-}0.17$) and depletion in immobile
272 HFSE ($\text{Nb/La} = 0.5\text{-}0.7$) typical for subduction-related magmas. Their incompatible trace
273 element patterns are similar to those of MSH andesites and dacites, but different from the
274 two basalt groups.

275 **Isotopic compositions**

276 Sr and Nd isotope compositions were determined for representative samples of the Castle
277 Creek period covering basaltic to dacitic compositions. Nd isotope compositions decrease
278 from $\epsilon_{\text{Nd}} = 7.7$ in the basalts to $\epsilon_{\text{Nd}} = 4.4$ in the dacites, whereas Sr isotope compositions
279 increase from about $^{87}\text{Sr}/^{86}\text{Sr} = 0.7030$ to 0.7038 (Fig. 6a). Both are in the range of isotopic
280 compositions of primitive Cascade basalts (Mullen and McCallum 2014) and are consistent
281 with literature data for MSH basalts and dacites (Halliday et al. 1983; Leeman et al. 1990).
282 There is no distinct difference in Sr and Nd isotope compositions between HFSE-rich
283 basalt and LKOT. $^{87}\text{Sr}/^{86}\text{Sr}$ ratios slightly increase with increasing whole-rock SiO_2 (Fig.
284 6b).

285 Whole-rock $\delta^{18}\text{O}$ values average at 5.7‰ in the basalts and 6.8‰ in the dacites (Fig. 6c).
286 They are comparable to values measured in earlier studies (Halliday et al. 1983; Leeman et
287 al. 1990). The two basaltic endmembers have similar $\delta^{18}\text{O}$ values in the range of MORB
288 ($5.5\text{-}5.9\text{‰}$, Bindeman 2008). $\delta^{18}\text{O}$ values increase with $^{87}\text{Sr}/^{86}\text{Sr}$ and whole-rock SiO_2
289 above the amount expected from closed-system differentiation (Fig. 6d) ($0.3\text{-}0.4\text{‰}$ for
290 fractionation from basalt to rhyolite, Bindeman 2008). $\delta^{18}\text{O}$ is always higher in plagioclase
291 ($5.8\text{-}6.8\text{‰}$) compared to whole-rock values, and lower in olivine ($5.1\text{-}5.7\text{‰}$). However,
292 the difference between minerals and whole-rocks is variable ($\Delta^{18}\text{O}_{\text{plg-wr}} = 0.1\text{-}1.1\text{‰}$ and
293 $\Delta^{18}\text{O}_{\text{wr-ol}} = 0.3\text{-}0.8\text{‰}$). $\Delta^{18}\text{O}_{\text{plg-ol}}$ values are scattering from 0.4 to 1.4‰ compared to 0.6-
294 0.8‰ expected from experimentally determined fractionation at $1200\text{-}1300\text{ °C}$ (Chiba et
295 al. 1989; Eiler 2001). This range is larger than that given for the average analytical
296 precision of $\pm 0.2\text{‰}$, suggesting that the phenocrysts analyzed are not in direct oxygen
297 isotope equilibrium for at least some of the samples.

298 **Petrography and mineral chemistry**

299 Most basalts and basaltic andesites of MSH are porphyritic (10-30 vol% crystals) with an
300 assemblage dominated by olivine and plagioclase (except for the basalt of the south flank,
301 which contains only a few percent of olivine in some flows). Chromian spinel occurs as
302 small inclusions in some olivine crystals. Some basaltic to basaltic andesitic flows (bsf,
303 bpc, bcc, mng) contain small, sparse clinopyroxene. The fine-grained matrices are
304 composed of plagioclase (plg), olivine (ol), clinopyroxene (cpx), titanomagnetite (mgt),
305 ilmenite (ilm), rare apatite (apt), and interstitial glass or, in the case of the tephra, a glassy
306 matrix. The Cave Basalt (LKOT endmember) differs texturally from HFSE-rich basalts by
307 a high abundance of glomerocrystic aggregates (Fig. 7a) that are rare in other basalts.
308 Petrographic descriptions of all Castle Creek units are given in Appendix A5.

309 **Plagioclase**

310 Plagioclase is the most abundant phase (5-30 vol%) in most mafic rocks. Sizes typically
311 range from microphenocrysts (tens of μm) to phenocrysts of 1-4 mm. Plagioclase
312 phenocrysts in the Cave Basalt (LKOT) are normally zoned with anorthite (An) contents
313 ranging from An₇₅ to An₆₀ (Fig. 8). Single crystals have the same compositions as those in
314 glomerocrystic aggregates suggesting entrainment of cognate crystal mush. In contrast, all
315 other mafic magmas contain complexly/reversely-zoned crystals (abundant in basalts, but
316 also common in arc-type basaltic andesites) in addition to usually smaller, normally zoned
317 varieties. They have low-An antecrystic cores (typically An₇₀₋₄₀, but reaching An₃₂) that
318 form dark areas on SEM images (Fig. 7b-d). These cores often have complex zonation
319 patterns, sieve-textured horizons or can be completely resorbed and replaced by a
320 microcrystalline mixture of plg, cpx, mgt, ilm, and glass. Rims of these reversely zoned
321 crystals show normal zoning with compositions similar to normally zoned phenocrysts
322 (An₇₈₋₆₄ in HFSE-rich basalts, An₇₄₋₄₄ in the arc-type basaltic andesite; Fig. 8). For
323 comparison, zoned plagioclase in the dacitic Bi tephra is restricted to compositions of
324 An₃₉₋₆₀, whereas the dacite of Red Rock Pass contains reversely zoned crystals with
325 compositions of An₄₁₋₆₅ and normally zoned crystals with An₈₀₋₆₄.

326 **Olivine**

327 Olivine is ubiquitous in all basalts and basaltic andesites (1-8 vol%). In general, the
328 crystals are normally zoned with a forsterite (Fo)-rich core and a thin (<10 μm) more
329 fayalite (Fa)-rich rim when in contact with the groundmass (Fig. 7a, e). This rim is lacking

330 when olivines are touching other grains, indicating rapid growth during final ascent,
331 extrusion and solidification of the basalts. Olivine crystals in arc-type basaltic andesite are
332 less abundant than in basalts and rimmed by orthopyroxene (Fig. 7f). Olivine compositions
333 range from Fo₈₆ to Fo₇₂ in HFSE-rich basalts, from Fo₈₁ to Fo₇₁ (with the majority of
334 crystal cores in a narrow range at Fo₇₇ to Fo₇₈) in LKOT, and from Fo₈₁ to Fo₅₈ in arc-type
335 basaltic andesite. Most olivine cores are close to equilibrium with their host rocks (Fig. 9).
336 Yet, the basalt of the south flank, the pre-Cave Basalt, and tephra layer Bu2 contain olivine
337 too Fo-rich and some Cave Basalt lava flows have olivine too Fa-rich to be in equilibrium.
338 NiO decreases relatively uniformly from about 0.3 wt% at Fo₈₆ to 0.03 wt% at Fo₆₀. In
339 contrast to other mafic units, the pre-Cave Basalt (LKOT group) and basalt of the south
340 flank (HFSE-rich basalt group) that both erupted from the southern flank contain at least
341 three populations of olivine (in order of abundance): normally zoned olivine (Fo₈₇-Fo₆₈)
342 with abundant Cr-spinel inclusions akin to olivine in HFSE-rich basalts, weakly zoned
343 olivine (Fo₇₉-Fo₇₃) with sparse spinel inclusions resembling olivine from the Cave Basalt
344 (LKOT), and sparse reversely zoned crystals (Fo₆₆-Fo₇₄).

345 **Chromian spinel**

346 Chromian spinel occurs as small inclusions (usually <20 μm) in olivine crystals. These are
347 abundant in olivine in HFSE-rich basalts, but rare in LKOT (Fig. 7a, e). Decreasing Fo
348 contents in olivine are accompanied by an increasing titano-magnetite component in the
349 spinel recognizable in higher Ti contents. Those with TiO₂ >2 wt% are excluded from
350 further discussion. This filter excludes spinel from the arc-type basaltic andesite of Nelson
351 Glacier that does not preserve spinel from the earliest stages of crystallization. The most
352 primitive spinels (Mg# >0.6; Mg# = Mg/(Mg+Fe) atomic ratio) in MSH basalts have Cr-
353 numbers (Cr# = Cr/(Cr+Al) atomic ratio) ranging from 0.15 to 0.4, similar to spinel from
354 southern Washington LKOT and HFSE-rich basalts (Fig. 9b, c), but below those of CAB
355 (>0.4, Baker et al. 1994; Clyne and Borg 1997; Smith and Leeman 2005). MSH LKOT
356 differs from southern Washington LKOT by slightly lower Cr#s (0.15 vs. 0.20 at
357 comparable Mg#, Smith and Leeman 2005) and higher V₂O₃ concentrations (0.3-0.6 vs.
358 0.1-0.2 wt.%, Smith and Leeman 2005).

359 The composition of primitive chromian spinel primarily depends on the lithology of the
360 mantle source and the degree of melting, i.e., the Cr-number decreases with source fertility

1
2
3
4
5
6
7
8
9
10
11
12
13
14
15
16
17
18
19
20
21
22
23
24
25
26
27
28
29
30
31
32
33
34
35
36
37
38
39
40
41
42
43
44
45
46
47
48
49
50
51
52
53
54
55
56
57
58
59
60
61
62
63
64
65

361 and increases with the degree of melting (Arai 1994; Clyne and Borg 1997). Individual
362 units form distinct trends on Cr# vs. Fo plots (Fig. 9b) that project backwards to different
363 lherzolite sources in the olivine spinel mantle array (*OSMA*, Arai 1994). Spinel Cr-
364 numbers in units of the HFSE-rich group weakly increase with decreasing Fo, whereas
365 those in LKOT endmember (Cave Basalt) show a steep increase and have the lowest Cr#
366 (Cr# = 0.15) in the most primitive (highest Mg#) spinels. The pre-Cave Basalt contains
367 two populations of spinel, each following one of the trends.

368 **Constraints on intensive parameters**

369 **Temperature**

370 Magmatic temperatures of MSH basalts were calculated from the most primitive (spinel
371 Mg# >60) olivine-spinel equilibrium pairs using the thermometer of Wan et al. (2008).
372 Olivine with spinel inclusions is assumed to crystallize under near-liquidus conditions
373 during transport and storage of magma in the crust. The highest temperatures (1235-1310
374 °C, ±22 °C) are obtained for the LKOT endmember (bc). They overlap with temperatures
375 (1170-1270 °C) of the HFSE-rich endmember (bnf/Bu2) and other units of the HFSE-rich
376 group (1120-1280 °C) (Fig. 10a). Within most units temperatures decrease with decreasing
377 spinel Mg#, consistent with progressive crystallization during cooling. As expected from
378 the most primitive phases, temperatures calculated from olivine-spinel pairs exceed those
379 derived from liquid, olivine-liquid and plagioclase-liquid thermometers for LKOT (1203-
380 1148 °C) and HFSE-rich basalts (1216-1112 °C) by Leeman and Smith (2018).

381 Storage temperatures just prior to eruption were derived from touching magnetite-ilmenite
382 pairs in HFSE-rich Bu basalt tephra. Seven pairs that fulfilled the equilibrium conditions
383 of Bacon and Hirschmann (1988) record temperatures from 850 to 1060 °C (±50 °C,
384 Sauerzapf et al. 2008). This range includes temperatures as low as observed in MSH
385 dacites (Gardner et al. 1995a) and likely reflects some assimilation of evolved material in
386 the mafic magma.

387 **Redox state**

388 The oxygen fugacity (fO_2) was determined using the olivine-spinel oxybarometer of
389 Ballhaus et al. (1990) and temperatures from the same contiguous pairs. Olivine and spinel
390 in the Cave Basalt (LKOT endmember) crystallized at an fO_2 relative to the quartz-

391 fayalite-magnetite (QFM) buffer of $\Delta\log(fO_2)^{QFM} = +0.1$ to $+0.4$ (average: QFM+0.2).
392 These conditions are slightly more reduced, but overlap in error (± 0.4 log units above
393 QFM) with those of HFSE-rich basalts and basaltic andesites ($\Delta\log(fO_2)^{QFM} = +0.5$ to $+1.1$,
394 average: QFM+0.8). More reduced conditions in LKOT are consistent with Fo contents in
395 olivine (Fig. 9) below those expected from whole-rock equilibrium (due to stabilization of
396 the Fe^{2+} -component) as well as lower Fe^{3+} and higher V concentrations in spinel at a given
397 Mg#. Melt $Fe^{3+}/\Sigma Fe$ ratios of 0.1-0.2 estimated from the experimentally determined
398 relationship between Fe^{2+}/Fe^{3+} in spinel and coexisting melt using the method of Maurel
399 and Maurel (1982) and Larsen and Pedersen (2000) confirm the relatively reduced
400 character of MSH basalts.

401 **Water content**

402 Water contents in the mafic magmas of MSH are challenging to measure. Most of the units
403 did not erupt explosively, precluding valuable estimates using melt inclusions. Olivine-
404 hosted melt inclusions in two tephra layers of the HFSE-rich basalt group gave H_2O
405 contents up to 2 wt% (Rea et al. 2012). Yet, the LKOT and arc-type endmember did not
406 erupt as tephra. The only other possible way of estimating H_2O content in these units are
407 mineral hygrometers. As those strongly rely on crystallization temperatures, which are
408 poorly known, we estimated H_2O contents from the Ca-Na exchange between plagioclase
409 and liquid (Sisson and Grove 1993). We used the most calcic plagioclase compositions
410 from cores of normally zoned crystals and outer zones of reversely zoned crystals and
411 whole-rock compositions as liquids. Ab-An exchange coefficients indicate equilibrium
412 between selected plagioclases and their host rocks (Putirka 2008), as do calculated
413 temperatures that overlap with plagioclase saturation temperatures within 5 °C (Putirka
414 2005). Comparison of plagioclase-whole-rock pairs with published partition coefficient
415 $((Ca/Na)_{plg}/(Ca/Na)_{liq})$ from Sisson and Grove (1993) suggest about ~ 1.8 H_2O in LKOT,
416 $\sim 3-4$ wt% H_2O in HFSE-rich basalts, and $\sim 3.5-4$ wt% H_2O in arc-type basaltic andesites
417 (Fig. 10b).

418 Estimated water contents in HFSE-rich basalt tephra exceed those measured in melt
419 inclusions, suggesting that melt inclusions might have been degassed prior to eruption
420 and/or that the method we used slightly overestimates H_2O . Assimilation of some more
421 evolved material could lead to an overestimation of the water content (e.g., assimilation of

1 422 15 % of water-rich dacite could add up to about 0.5 wt% H₂O). Our estimates also exceed
2 423 hygrometric estimates for MSH LKOT and HFSE-rich basalts by Leeman and Smith
3 424 (2018). Using their approach of iterative calculation of pressure, temperature, and water
4 425 content at a defined *equilibrium* plagioclase composition (for details see Leeman and
5 426 Smith 2018), our samples yield 0.4-0.9 wt% H₂O in LKOT, negligible amounts of water in
6 427 the HFSE-rich basalt endmember (bnf/Bu2), 0.3-1.3 wt% H₂O in other units of the HFSE-
7 428 rich basalt group, and 2.0-2.4 wt% in the arc-type basaltic andesite of Nelson Glacier. As
8 429 arc-type basaltic andesites are not saturated with olivine (as required by the method),
9 430 predicted temperatures in this unit are likely overestimated and water contents respectively
10 431 underestimated. In addition, the *equilibrium* plagioclase composition defined by the
11 432 method of Leeman and Smith (2018) is shifted to the sodic side of the spectrum embracing
12 433 xenocrystic cores, which might further underestimate the water content. Combining
13 434 evidence from the two methods suggests low to moderate H₂O concentrations in LKOT
14 435 and HFSE-rich basalts, and a range between 2 and 4 wt% H₂O in arc-type basaltic
15 436 andesites.

16 437 **Discussion**

17 438 Throughout the past 40 years various studies have discussed the diversity of primitive
18 439 magmas in the Cascades; typically using radiogenic isotopes, experiments, reconstruction
19 440 of primary melt compositions and/or primitive minerals to characterize mantle source
20 441 compositions (e.g., Bacon 1990; Leeman et al. 1990; Bartels et al. 1991; Baker et al. 1994;
21 442 Bacon et al. 1997; Borg et al. 1997; Clyne and Borg 1997; Conrey et al. 1997; Reiners et
22 443 al. 2000; Grove et al. 2002; Leeman et al. 2005; Smith and Leeman 2005; Hildreth 2007;
23 444 Schmidt et al. 2008; Rowe et al. 2009; Moore and DeBari 2012; Mullen et al. 2017). These
24 445 studies considered *primitive* magmas to have low phenocryst contents (<5 %, olivine ±
25 446 spinel), olivine compositions close to mantle values (Fo ≥86), Mg# ≥0.6, MgO >8 wt%,
26 447 and high compatible trace element contents (Cr >200 ppm, Ni >100 ppm) (Mullen et al.
27 448 2017). Mafic magmas of MSH deviate from these criteria by their high crystallinities
28 449 (usually 10-30 %), abundant plagioclase crystals with disequilibrium textures and sodic
29 450 cores in most basalts, several populations of olivine and spinel in some basalts, and their
30 451 overall more evolved whole-rock (MgO 4.0-7.4 wt%, Cr 40-240 ppm, and Ni 35-140 ppm)
31 452 and mineral compositions (Fo ≤81-87) (Table 2). However, the most mafic endmembers

1
2
3
4
5
6
7
8
9
10
11
12
13
14
15
16
17
18
19
20
21
22
23
24
25
26
27
28
29
30
31
32
33
34
35
36
37
38
39
40
41
42
43
44
45
46
47
48
49
50
51
52
53
54
55
56
57
58
59
60
61
62
63
64
65

453 still preserve their characteristic mantle-derived signatures with strong compositional
454 similarities to more primitive variants in the Cascades (Fig. 2-5) as well as nearly primitive
455 chromian spinel (Fig. 9b, c) allowing for some interpretation of their origin. In the
456 following, we will discuss deviations from the endmember classification of previous
457 studies at MSH (Smith and Leeman 1993; Leeman and Smith 2018) and modifications of
458 these non-primitive magmas by crustal processes, evaluate pre-existing hypotheses on their
459 mantle origin, and finally, discuss the implications for the MSH magma plumbing system.

460 **Three mafic endmembers at Mount St. Helens**

461 Despite its arc setting and the predominant eruption of hydrous dacites, true arc basalt did
462 not erupt from MSH. Previous studies (Smith 1984; Leeman et al. 1990; Smith and
463 Leeman 1993; Leeman et al. 2005; Smith and Leeman 2005; Leeman and Smith 2018) also
464 described *LKOT* and *HFSE-rich basalt* at MSH. The origin of calc-alkaline basaltic
465 andesites was predominantly attributed to mixing (Leeman and Smith 2018), similar to that
466 of many andesites at MSH (Pallister et al. 1992; Smith and Leeman 1993). However, our
467 third endmember (*arc-type basaltic andesite*) differs from previously described (low-SiO₂)
468 calc-alkaline basaltic andesites that form nearly continuous geochemical trends from
469 LKOT and HFSE-rich basalts towards basaltic andesite. In contrast to these rocks, the
470 newly described arc-type basaltic andesites are slightly more evolved, have lower contents
471 of FeO, TiO₂, and P₂O₅, typical of Cascade CAB (Fig. 3), and show a pronounced arc
472 signature (i.e., enrichment in fluid-mobile LILE and LREE relative to HFSE and HREE;
473 Fig. 5, Table 2). Arc-type basaltic andesites show some disequilibrium textures, as
474 expected from mafic magma crossing a silicic mush system, but at least in the *basaltic*
475 *andesite of Nelson Glacier (mng)* these are minor (Appendix A5). This unit contains a
476 single population of olivine with cores that are close to equilibrium with its whole-rock
477 composition (Fig. 9a). In addition, it has lower concentration of Nb and strongly
478 incompatible elements (e.g., K, Rb, Ba, Ca) than Castle Creek andesites or dacites and has
479 the highest Al₂O₃ content of Castle Creek rocks, both excluding a predominant mixing
480 origin. The presence of melts with compositions similar to the basaltic andesite of Nelson
481 Glacier at depth is further supported by equilibrium melts calculated from amphibole
482 compositions (Wanke, unpublished data). These rocks are not primitive, but represent the
483 most mafic endmember of the calc-alkaline rock series at MSH.

484 **Petrogenetic processes influencing the chemical composition of mafic endmembers**

485 *Fractional crystallization*

486 The high crystallinity of MSH basalts (10-30 %) and evidence for contamination prevent
487 reconstruction of mantle-derived melts. Yet fractionation of olivine and spinel is evident
488 from compositional trends formed by these minerals (Fig. 9). Weakly increasing Cr# with
489 decreasing Mg# in most of the spinel is a function of decompression and crystallization of
490 olivine (\pm spinel), whereas the strong increase in spinel Cr# with decreasing Mg# in the
491 Cave Basalt indicates that this compositional change was dominated by decompression
492 rather than melt differentiation and/or accompanied by co-crystallizing plagioclase (e.g.,
493 Clyne and Borg 1997; Smith and Leeman 2005). However, the lack of significant Eu
494 anomalies in MSH basalt and basaltic andesite demonstrates that plagioclase was not a
495 major early fractionating phase. Instead, it mostly crystallized late and has not
496 significantly fractionated from the magma. Scattered Eu/Eu* (0.92-1.08) within some
497 mafic units likely results from mineral proportions in the respective rock sample.

498 Trace element variations exclude a genetic relationship between the mafic endmembers by
499 fractional crystallization. HFSE-rich basalts have higher abundances of most incompatible
500 trace elements than more evolved magmas (Fig. 4, 5). LKOT have similar abundances of
501 HFSE and higher abundances of HREE than arc-type basaltic andesite. As incompatible
502 elements would increase during fractionation, both basalt types can be excluded as parental
503 magmas for arc-type basaltic andesites. Likewise, Leeman and Smith (2018) have shown
504 that fractional crystallization cannot reproduce compositions of low-SiO₂ basaltic andesites
505 from HFSE-rich basalt or LKOT. Instead, they suggested that mixing between distinct
506 primitive Cascade basalts and intermediate material similar to MSH andesite
507 predominantly formed compositional trends from HFSE-rich basalt and LKOT towards
508 low-SiO₂ basaltic andesite.

509 *Assimilation and mixing in a polybaric mush column*

510 Isotopic, chemical, and textural characteristics of mafic magmas at MSH indicate
511 interaction with various assimilants including pre-existing crustal lithologies and
512 antecrystic material. The total isotopic variation between basalts and dacites is small, but
513 significant ($^{87}\text{Sr}/^{86}\text{Sr} = 0.7030\text{-}0.7038$, $\epsilon_{\text{Nd}} = 7.7\text{-}4.4$, $\delta^{18}\text{O} = 5.7\text{-}6.8$ ‰). The correlation of

1
2
3
4
5
6
7
8
9
10
11
12
13
14
15
16
17
18
19
20
21
22
23
24
25
26
27
28
29
30
31
32
33
34
35
36
37
38
39
40
41
42
43
44
45
46
47
48
49
50
51
52
53
54
55
56
57
58
59
60
61
62
63
64
65

514 radiogenic Sr and Nd isotopes and with SiO₂ (Fig. 6a, b) as well as an increase in δ¹⁸O
515 above the array expected from closed system fractionation (Fig. 6c, d) indicates that some
516 crustal assimilation (assimilant with high ⁸⁷Sr/⁸⁶Sr, low ε_{Nd}, and high δ¹⁸O) is involved
517 during magma evolution. A quantitative interpretation of these isotope trends remains
518 ambiguous owing to the unknown age of the (probably accretionary) lower crustal
519 basement and the young (Tertiary) age of the upper crust (Hildreth 2007). The correlation
520 of δ¹⁸O in olivine with whole-rock SiO₂ suggests that some assimilation happens during
521 early crystallization at depth.

522 Mafic magmas erupting in close spatial and temporal proximity with andesite and dacite at
523 MSH would likely interact with pre-existing magmas or mush zones that plug the
524 magmatic pathways. Most basalts and basaltic andesites contain plagioclase phenocrysts
525 with sodic cores and/or various resorption textures (Fig. 7b-d) that represent relics of this
526 process. Core compositions of reversely zoned plagioclase from An₄₀ to An₇₀ (in some
527 cases down to An₃₂; Fig. 8) are consistent with crystallization from andesitic to rhyolitic
528 melts. The wide range in δ¹⁸O values of plagioclase separates with some values higher than
529 those expected from closed system fractionation, and hence also large range in Δ¹⁸O_{plg-ol}
530 (Fig. 6d), support the chemical and textural evidence for assimilation of more evolved
531 (higher δ¹⁸O) material within the mafic magma. Other associated mineral phases from this
532 crystal-rich dacite (e.g., amphibole ± pyroxene ± apatite ± oxides) would have been
533 unstable in the basaltic magmas and dissolved and/or partly re-equilibrated. This is
534 supported by sparse, sometimes resorbed pyroxene and hornblende xenocrysts in some of
535 the basalts and basaltic andesites. Furthermore, the wide range of temperatures recorded by
536 Fe-Ti oxides in Bu tephra (1060-850 °C) that includes low temperatures as observed in
537 MSH dacite indicates late stage assimilation of evolved material without time for
538 equilibration of oxides. This observation is consistent with rare *blebs* of rhyolitic glass in
539 basalt described by Smith and Leeman (1993) and Leeman and Smith (2018). Assimilation
540 and mixing processes are exemplified by the eruption sequences on the southern and
541 northern flanks of the volcano.

542 *Sequence of eruptions on the southern flank*

543 The sequence of eruptions on the southern flank well illustrates the interaction between
544 different basalts and dacite in the upper crustal system. Evidence for mixing between

1
2
3
4
5
6
7
8
9
10
11
12
13
14
15
16
17
18
19
20
21
22
23
24
25
26
27
28
29
30
31
32
33
34
35
36
37
38
39
40
41
42
43
44
45
46
47
48
49
50
51
52
53
54
55
56
57
58
59
60
61
62
63
64
65

545 distinct mafic endmembers is mostly absent, with exception of the pre-Cave Basalt (LKOT
546 group) and the basalt of the south flank (HFSE-rich basalt group). The pre-Cave Basalt
547 contains multiple populations of olivine and spinel (Fig. 9), respectively similar to those of
548 the basalt of the southern flank and the Cave Basalt (LKOT), and has compositions
549 encompassing the high-K and low-K trends (Fig. 3, 4). Evidence for mixing between the
550 two basalt groups is reinforced by the stratigraphic position of the pre-Cave Basalt
551 between the Cave Basalt and the basalt of the southern flank (Table 1).

552 Sodic plagioclase cores in the pre-Cave Basalt represent relics of entrained more evolved
553 material, but the basalt of the south flank is crystal-poor (2-5 % crystals). Thus, it must
554 have largely remelted the pre-existing crystal mush. That is supported by the preceding
555 almost aphyric (<3 % crystals) dacite of Red Rock Pass. It contains rare remnants of
556 reversely zoned, almost completely resorbed plagioclase crystals and rare normally zoned
557 crystals with basaltic core compositions (An_{82-72} , Fig. 8). These observations indicate
558 strong heating and mixing between a basaltic and a dacitic component before eruption. The
559 incoming basalt of the south flank might have heated the pre-existing dacite and forced it
560 out of the shallow reservoir. Subsequently, the basalt ascended into the shallow reservoir
561 that was mostly evacuated of magma allowing it to erupt crystal-poor. The incoming Cave
562 Basalt (LKOT) mixed with the residual basalt of the south flank (here basaltic andesite) to
563 form the heterogeneous pre-Cave Basalt. This again cleared the conduit to allow the Cave
564 Basalt magma to crystallize its characteristic assemblage of olivine and plagioclase with
565 normal zoning and erupt almost unaffected by silicic magma.

566 *Sequence of eruptions on the northern flank*

567 Three magmatic cycles of dacite to andesite to basalt/basaltic andesite similar to those first
568 suggested by Hopson and Melson (1990) and discussed by Pallister et al. (1992) erupted on
569 the northern and northeastern flanks of the volcano during the late Castle Creek period
570 (Table 1). This cyclic behavior exemplifies how basalts pave their way through the upper
571 crustal silicic reservoir. It is considered to be caused by basalt intrusion and mixing with
572 resident dacite to produce andesite, followed by a less mixed olivine-bearing basaltic
573 andesite, followed by basalt that retains sodic plagioclase cores as the only evidence for
574 mixing (e.g., eruptive sequence a26-mtt-bnf, Appendix A5). The units in these cycles
575 display decreasing phenocryst disequilibrium and SiO_2 content as the cycle proceeds,

1
2
3
4
5
6
7
8
9
10
11
12
13
14
15
16
17
18
19
20
21
22
23
24
25
26
27
28
29
30
31
32
33
34
35
36
37
38
39
40
41
42
43
44
45
46
47
48
49
50
51
52
53
54
55
56
57
58
59
60
61
62
63
64
65

576 producing the observed compositional trends from basaltic andesite to basalt. Eventually,
577 part of the system is cleaned of intermediate compositions, which permits basalt to ascend
578 with only minor interaction with the shallow system. Similarly, Leeman and Smith (2018)
579 describe stratigraphic sequences of lava flows of single units (HFSE-rich basalts) that
580 become progressively less evolved towards the top (upward increase in Mg#). Their
581 calculations indicate that the compositional ranges observed in MSH LKOT and HFSE-
582 rich basalts are dominantly caused by mixing of primitive Cascade basalts with different
583 amounts of more evolved calc-alkaline material with compositions similar to MSH
584 andesite. This interpretation is in agreement with our data.

585 **Origin of the mafic endmembers of Mount St. Helens**

586 The challenge in deciphering the origin of MSH basalts is to see through the contamination
587 processes. Chromian spinel is the first crystallizing phase in most mafic magmas from
588 MSH. It only crystallizes from relatively primitive liquids, and thus, is expected to
589 crystallize before the melt was significantly affected by assimilation. Similar spinel
590 compositions of genetically related basalts and peridotites (e.g., Dick and Bullen 1984)
591 allow for some constraints on the mantle sources of the basalts. Spinel Cr# increases as the
592 peridotite source becomes more refractory; i.e., harzburgite typically contains spinel with
593 Cr# >0.5, whereas lherzolite has spinel with Cr# <0.5 (Arai 1994). Increasing degree of
594 (hydrous) melting would further increase the Cr#. The impact of other parameters, such as
595 pressure, fO_2 , and fractionation or mixing, on the spinel Cr# is usually less than a few
596 percent (Clynne and Borg 1997). In addition to the investigation of primitive phases,
597 striking geochemical similarities between the most mafic endmembers of each type and
598 more primitive Cascade basalts (Fig. 3-5) allow for some further constraints on their
599 origin.

600 *HFSE-rich basalts*

601 Each unit within the HFSE-rich basalt group contains chromian spinels with distinct
602 compositions. They form almost linear trends caused by melt differentiation that allow for
603 back projection to the OSMA (Fig. 9b, c) and indicate lherzolite mantle sources (Cr# <0.4)
604 for all units. Cr-numbers in the most primitive spinels (Mg# >0.6) are lowest in the HFSE-
605 rich endmembers, the basalt of the north flank (Cr# = 0.25), and increase towards the
606 basalt of Castle Creek (Cr# = 0.3) and the basalt of the south flank (Cr# = 0.35-0.4). As the

1
2
3
4
5
6
7
8
9
10
11
12
13
14
15
16
17
18
19
20
21
22
607 effect of pressure, fO_2 , fractionation, or mixing on spinel compositions is too small to
608 explain this variation in spinel Cr# (Clynne and Borg 1997), the increase in Cr# implies
609 decreasing source fertilities and/or increasing degrees of melting. The HFSE-rich basalt
610 endmember has the highest incompatible element concentrations (Fig. 3-5) consistent with
611 the lowest spinel Cr# and the lowest degree of melting. Our data agree with previous
612 studies of HFSE-rich basalts in the Cascades that suggest an origin by low-degree partial
613 melting (usually 1-5 %) of an enriched, fertile mantle source (Leeman et al. 1990; Bacon et
614 al. 1997; Conrey et al. 1997; Reiners et al. 2000; Leeman et al. 2005; Smith and Leeman
615 2005; Jicha et al. 2009; Rowe et al. 2009). Their steep REE patterns are usually assigned to
616 residual garnet in the source. High La/Yb (9.3-12.9) and Dy/Yb (2.0-2.3) ratios (Fig. 11c,
617 d; Table 2) in HFSE-rich basalts at MSH are consistent with an origin by low-degree
618 melting in the stability field of garnet.

23
24
25
26
27
28
29
30
31
32
33
34
35
36
37
38
39
40
41
42
43
44
45
46
47
48
49
619 Spinel Cr-numbers and trace element abundances in whole-rocks suggest variable
620 contributions of a subduction component to different units of the HFSE-rich basalt group.
621 Low water contents (up to 2 wt.% H_2O in olivine-hosted melt inclusions in Bu2 and Bu3
622 tephra; Rea et al. 2012), high magmatic temperatures (Fig. 10), and the lack of a
623 pronounced arc signature in these rocks (Fig. 5) imply comparably dry conditions during
624 melting. Yet, Cr-numbers in the most primitive spinels of the basalt of the south flank
625 nearly approach those of Cascade CAB (Fig. 9b, c) implying higher degrees of partial
626 melting and a potentially greater subduction component. They are inversely correlated with
627 Nb and Nb/La that decrease (at comparable MgO) from the basalt of the north flank to the
628 basalt of Castle Creek to the basalt of the south flank (Fig. 4, 5) supporting an increasing
629 (albeit minor) subduction component in these units. Such an interpretation is consistent
630 with studies that suggest a correlation between the degree of melting and the addition of a
631 slab-derived component in Cascade basalts (Borg et al. 1997; Reiners et al. 2000; Rowe et
632 al. 2009).

50
51
52
53
54
55
56
57
58
59
60
61
62
63
64
65
633 *LKOT*

634 Spinel in LKOT from MSH has low Cr-numbers (Cr# = 0.15 at highest Mg#, Fig. 9c)
635 indicative of a highly fertile (i.e., rich in Al, Ca, and Fe, high capability to produce melt,
636 Clynne and Borg 1997) lherzolite source, consistent with comparably high contents of Al,
637 Ca, and Fe in whole-rocks (Fig. 3). Although high Ca and Al can also result from

1
2
3
4
5
6
7
8
9
10
11
12
13
14
15
16
17
18
19
20
21
22
23
24
25
26
27
28
29
30
31
32
33
34
35
36
37
38
39
40
41
42
43
44
45
46
47
48
49
50
51
52
53
54
55
56
57
58
59
60
61
62
63
64
65
638 accumulation of plagioclase (which is abundant in glomerocrysts in the Cave Basalt), low
639 Sr and the lack of a Eu-anomaly in LKOT as well as high Ca and Al in more primitive
640 Cascade LKOT suggest that this signature is rather a source characteristic than the result of
641 crystal accumulation. The most primitive spinels in LKOT have lower Cr-numbers ($Cr\# =$
642 0.15) than those in HFSE-rich basalts ($Cr\# = 0.25-0.4$) pointing to a more fertile source
643 and/or lower degrees of melting in LKOT (Fig. 9c, d). Both are inconsistent with lower
644 abundances of incompatible trace elements in LKOT that require a more trace element
645 depleted source and/or higher degrees of melting (Fig. 11b). This discrepancy indicates
646 that MSH LKOT must be derived from a compositionally different (less enriched)
647 lherzolite source than HFSE-rich basalts.

648 Slight enrichments in LREE and LILE over HREE and HFSE (Fig. 5, 12) point a weak
649 subduction component in MSH LKOT. As good constraints on water contents in MSH
650 LKOT are lacking, it remains speculative whether this signature represents a recent
651 subduction component or was inherited in the source during ancient subduction times.
652 Hygrometric estimates of water content suggest up to 1.8 wt% H_2O in the Cave Basalt
653 (Fig. 10b), illustrating that some contribution of a recent subduction component may be
654 reasonable. However, high magmatic temperatures (up to 1300 °C, Fig. 10a) and
655 comparatively reduced conditions (around QFM+0.2) in MSH LKOT require low water
656 contents and high crustal pressure during early crystallization of olivine and spinel,
657 suggesting that our water contents are likely overestimated for LKOT. That is further
658 supported by nearly anhydrous conditions suggested from experimental constraints
659 (Bartels et al. 1991) and olivine-hosted melt inclusions (Sisson and Layne 1993; Le Voyer
660 et al. 2010) in southern Cascade LKOT. These are generally interpreted as dry,
661 decompression-induced melts (Leeman et al. 1990; Bartels et al. 1991; Bacon et al. 1997;
662 Elkins-Tanton et al. 2001; Leeman et al. 2005), derived by 6-10 % of partial melting in the
663 Mt. Shasta region (Baker et al. 1994) and from <10 % in the northern to 20-30 % in the
664 southern central Cascades (Conrey et al. 1997). Along with previous interpretations and
665 the position of MSH in an extensional regime (Weaver et al. 1987), we interpret our data to
666 reflect an origin of MSH LKOT by dominantly decompression-induced melting of a fertile
667 lherzolite source. The lack of HREE depletion in LKOT (Fig. 5; Table 2) is consistent with
668 a garnet-free source in the upper mantle.

669 *Arc-type basaltic andesites*

1
2 670 As arc-type basaltic andesites at MSH contain only 3.9-5.2 wt% MgO and lack primitive
3
4 671 spinel, a mantle-derived parent remains poorly constrained. A direct mantle origin of these
5
6 672 basaltic andesites, as suggested for primitive high-Mg basaltic andesites in the Shasta and
7
8 673 Lassen regions (Baker et al. 1994; Clynne and Borg 1997; Conrey et al. 1997; Grove et al.
9
10 674 2002) or for some non-primitive variants at Mt. Baker and Glacier Peak (Moore and
11
12 675 DeBari 2012; Mullen and McCallum 2014; Sas et al. 2017), can be excluded based on their
13
14 676 comparably evolved whole-rock and mineral compositions ($Fo \leq 81$ in olivine, $An \leq 75$ in
15
16 677 plagioclase). Along with the chemical subduction signature and high estimated water
17
18 678 contents, these characteristics rather suggest a derivation by differentiation of a CAB-like
19
20 679 precursor, as observed in other places in the Cascades (e.g., Kinzler et al. 2000; Hildreth
21
22 680 2007; Moore and DeBari 2012).

23 681 Arc-type basaltic andesites at MSH show a pronounced arc signature with enrichment in
24
25 682 fluid-mobile over immobile trace elements and negative Nb-Ta-anomalies (Fig. 5, 11;
26
27 683 Table 2), yet the origin of such compositions in Cascade basalts is still debated. Most
28
29 684 studies agree upon an origin of Cascade CAB and BA by flux melting (~10-30 % partial
30
31 685 melting) of a variably depleted mantle source (Bacon et al. 1997; Reiners et al. 2000;
32
33 686 Grove et al. 2002; Hildreth 2007; Rowe et al. 2009; Moore and DeBari 2012; Mullen et al.
34
35 687 2017). That is confirmed by olivine-hosted melt inclusions with water contents up to 3.6
36
37 688 wt% (Sisson and Layne 1993; Le Voyer et al. 2010; Ruscitto et al. 2010) and experimental
38
39 689 constraints on southern Cascade CAB (Baker et al. 1994). In contrast, Leeman et al. (2004)
40
41 690 and Leeman et al. (2005) concluded from estimated mantle segregation pressures and
42
43 691 temperatures and the depletion of light volatile B and Li in southern Washington basalts
44
45 692 that the young and hot slab almost completely dehydrates beneath the forearc.
46
47 693 Consequently, they proposed that partial melting in the mantle wedge is dominantly dry
48
49 694 and the subduction signature in CAB and BA could be inherited from a mantle source
50
51 695 metasomatized during ancient stages of Cascade subduction. However, depletion of light
52
53 696 volatile B is also observed in the Lassen (Walowski et al. 2016) and Shasta regions (Rose
54
55 697 et al. 2001; Le Voyer et al. 2010) of the arc, nevertheless those basalts contain significant
56
57 698 hydrous slab components. Walowski et al. (2016) explained this discrepancy with a fluid

699 source in the sub-slab mantle rather than in the slab itself, which might also be the case in
700 the southern Washington area.

701 The distinction between an origin of the subduction signature in MSH arc-type basaltic
702 andesites from recent flux melting or from an ancient subduction component stored in the
703 mantle requires the knowledge of water content. Plagioclase hygrometry suggests H₂O
704 content between 2 and 4 wt% H₂O. We argue that the upper end is more likely, because
705 these basaltic andesites have high Al₂O₃ and low FeO and TiO₂ compared to other mafic
706 units at MSH (Fig. 3), supporting higher water contents in these rocks. Crystallization
707 under hydrous conditions leads to the suppression of plagioclase and early appearance of
708 Fe-Ti oxides in the crystallizing mineral assemblage, resulting in higher Al₂O₃ and lower
709 FeO and TiO₂. In addition, the presence of a hydrous mafic endmember is supported by
710 water contents up to 6-7 wt% in MSH dacites (Gardner et al. 1995b; Blundy and Cashman
711 2005; Blundy et al. 2008). Blatter et al. (2017) have shown by mass-balance calculations
712 based on experiments on MSH dacite that regular recharge of the system by H₂O-rich
713 basalt or basaltic andesite is necessary to induce persistent production of hydrous dacite
714 liquid in the mid to lower crust. Thus, we interpret arc-type basaltic precursors of these
715 magmas to result from flux melting of a peridotite source. As primitive compositions are
716 not preserved, it is not possible to determine whether this source is distinct from those of
717 LKOT or HFSE-rich basalt or affected by a greater contribution of a hydrous slab-derived
718 component. Comparably high abundances of (even fluid immobile) trace elements indicate
719 that all basalt types at MSH derived from mantle sources more enriched than that of N-
720 MORB (Fig. 5, 11).

721 *Heterogeneity of the mantle*

722 The heterogeneity of mantle sources beneath MSH is at least partly caused by the
723 accretionary history of the arc. The oceanic Siletzia terrane accreted about 50 Ma ago to
724 the North American border (Wells et al. 2014), likely influencing the oceanic affinity
725 (including OIB- and E-MORB-like rocks) of many Cascade basalts. In addition, upwelling
726 asthenospheric mantle, as suggested as a source for HFSE-rich basalts in the Mt. Adams-
727 Simcoe back-arc region (Mullen et al. 2017), might contribute to the heterogeneity in the
728 mantle wedge (Fig. 12a). Indeed, seismic tomography indicates a gap or tear in the slab
729 beneath northern Oregon providing a potential pathway for upwelling enriched sub-slab

1
2
3
4
5
6
7
8
9
10
11
12
13
14
15
16
17
18
19
20
21
22
23
24
25
26
27
28
29
30
31
32
33
34
35
36
37
38
39
40
41
42
43
44
45
46
47
48
49
50
51
52
53
54
55
56
57
58
59
60
61
62
63
64
65

730 mantle (Schmandt and Humphreys 2010; Martin-Short and Allen 2013). Alternatively,
731 Hansen et al. (2016) suggested that the melt source region lies east towards Mt. Adams and
732 migrates into the mantle beneath MSH.

733 The close spatial and temporal eruption of different mafic endmembers (within <5 km and
734 150 years) at MSH requires simultaneous tapping of different mantle sources and different
735 melting mechanisms acting over short distances. This is of particular interest, as the slab
736 reaches only a depth of about 70 km beneath MSH (McCroory et al. 2012), just approaching
737 the depth range of hydrous mineral break-down and water release (Schmidt and Poli 1998).
738 LKOT and HFSE-rich basalts derived from at least two distinct, variably trace element
739 enriched, fertile lherzolite sources. Their origin is dominated by decompression melting
740 with only minor contributions of a subduction component. In addition, CAB-like
741 precursors of arc-type basaltic andesites are derived by flux melting from a similar or an
742 additional mantle source. According to the limited space in the mantle wedge and the
743 evidence for variable (although minor) amounts of subduction components in different
744 units of the HFSE-rich basalt group, these likely derived from the water-poor periphery of
745 the main flux melting regime, potentially tapping an enriched source (Fig. 12a).

746 **Implications for the Mount St. Helens magma plumbing system**

747 *Ascent through the crust*

748 The close temporal and spatial eruptions of different basalt types, andesites and dacites
749 have important implications for the geometry of the MSH magma plumbing system. When
750 associated with intermediate to silicic stratovolcanoes, basalts are typically restricted to the
751 periphery of these systems (e.g., Hildreth 2007). The reasons are mush zones in the crust
752 that induce a *shadow zone* on the surface. They form rheological and lithological barriers
753 that intercept ascending denser mafic magmas (Dufek and Bergantz 2005; Karlstrom et al.
754 2009; Kent et al. 2010). Yet at MSH true basalt erupted through the axial system. Some
755 vents of the basalt of the north flank are directly associated with dacitic lava domes (e.g.,
756 Dogs Head dome) and some dykes of the basalt of Castle Creek are observed in the 1980
757 crater walls. The apparent lack of a *shadow effect* suggests that some basalts might largely
758 bypass the major plumbing system. Recent seismic investigations indicate a high velocity
759 zone in the lower crust vertically beneath MSH and a low velocity zone about 10-20 km

1
2
3
4
5
6
7
8
9
10
11
12
13
14
15
16
17
18
19
20
21
22
23
24
25
26
27
28
29
30
31
32
33
34
35
36
37
38
39
40
41
42
43
44
45
46
47
48
49
50
51
52
53
54
55
56
57
58
59
60
61
62
63
64
65

760 southeast of the volcano; the latter interpreted as a lower crustal storage zone with
761 dispersed melt (Kiser et al. 2016). Magnetotelluric data further supports the location of a
762 lower crustal mush zone east of MSH (Bedrosian et al. 2018). Such an offset geometry of
763 the magmatic system (Fig. 12a) facilitates the upward migration of basalt aside from main
764 lower crustal plumbing system and agrees with the simultaneous generation of dacites in a
765 mid to lower crustal mush zone (at about 700-900 MPa, Blatter et al. 2017).

766 Different mafic units have distinct chromian spinel compositions and show variations in
767 source fertility and/or degree of partial melting (Fig. 9b, c). Thus, they require extraction
768 from the mantle and ascent through the crust as individual batches of magma (except from
769 the mixed pre-Cave Basalt). Models of dynamic melt transport in the mantle suggest that
770 melts are transported in a network of channels that converge close to the base of the crust
771 (e.g., Kelemen et al. 1997; Spiegelman and Kelemen 2003). Channelized transport allows
772 for the concurrent existence of variable melt compositions in a restricted area; potentially
773 leading to peripheral channels transporting compositionally different (e.g., water-poorer)
774 melts. Although much of that melt might get absorbed by the lower crustal mush zone or
775 freeze during transport, some would eventually be extracted from marginal melt channels
776 aside from the main focus region of the channel network, facilitated by the proposed offset
777 geometry of the plumbing system (Fig. 12a) (Kiser et al. 2016). Weak crustal zones
778 associated with the fracture system beneath MSH (Weaver et al. 1987) might then serve as
779 conduits for fast and nearly isolated transport of individual magma batches that prevents
780 them from mixing, stalling, and freezing in the crust. That is consistent with the common
781 occurrence of different basalt types associated with fracture systems in the Cascades (e.g.,
782 Leeman et al. 1990; Hildreth 2007; Muffler et al. 2011).

783 *Interaction with the shallow crustal system*

784 Geochemical mixing trends from basalt to basaltic andesite within individual units as well
785 as relics of more evolved material illustrate the interaction of basalt with the upper crustal
786 part of the system. Distinct compositions of entrained plagioclase cores in individual mafic
787 units indicate that the ascending magmas assimilate variably evolved magma/mush on their
788 way to the surface (e.g., the pre-Cave Basalt contains more evolved plagioclase cores than
789 the basalt of the north flank, Fig. 8). This observation indicates that different units take
790 individual pathways through the upper crustal reservoir, while tapping compositionally

1
2
3
4
5
6
7
8
9
10
11
12
13
14
15
16
17
18
19
20
21
22
23
24
25
26
27
28
29
30
31
32
33
34
35
36
37
38
39
40
41
42
43
44
45
46
47
48
49
50
51
52
53
54
55
56
57
58
59
60
61
62
63
64
65

791 different (more evolved), melt-rich regions (Fig. 12b, c). This interpretation is consistent
792 with recent seismic imaging that shows accumulation of melt (up to 10-12 vol.%) in
793 laterally dispersed, vertically interconnected lenses within a mush-filled reservoir (Kiser et
794 al. 2018), although the geometry might have been slightly different during Castle Creek
795 time.

796 The difficulty of crossing this mush-filled reservoir is illustrated by the restriction of basalt
797 eruptions to a short interval during the Castle Creek period (1700-1900 B.P.). Except for
798 olivine-bearing mafic inclusions in a Cougar age (18-28 ka B.P.) lava flow and olivine-
799 bearing Mo tephra (Clynne et al. 2008), there is evidence for mafic magma (in form of
800 mafic inclusions) in the shallow magmatic system from 2.6 to 0.2 ka (from Pine Creek to
801 Kalama eruptive periods). The reason for the sudden appearance of basaltic magma in the
802 shallow magma system from Pine Creek to Kalama times remains speculative. There is no
803 supporting evidence for a change in the crustal stress field in the MSH area or a major
804 edifice collapse during Pine Creek time, as proposed for the initiation of basaltic
805 volcanism at similar systems (e.g., South Soufrière Hills, Cassidy et al. 2015). However, in
806 agreement with the location of MSH along a tensional pull-apart basin associated with an
807 offset in the St. Helens seismic zone (Weaver et al. 1987), it seems likely that a change in
808 the crustal stress regime (such as an extensional tectonic event leading to re-activation of
809 old fracture zones) enabled basalts to reach shallow crustal levels.

810 **Conclusions**

811 Detailed chemical and petrological investigations of eight mafic units from MSH that
812 erupted during a short interval at the end of the Castle Creek period (1900-1700 years
813 B.C.) reveal three mafic endmembers including HFSE-rich basalts, LKOT and arc-type
814 basaltic andesites, each resembling more primitive variants in the Cascades. Some of the
815 heterogeneity in mafic compositions clearly results from fractional crystallization, magma
816 mixing, and assimilation of old crustal and young more evolved calc-alkaline material at
817 different depths. However, the variability of the most mafic endmembers still requires at
818 least two distinct mantle sources and different contributions from a slab-derived
819 component.

1
2
3
4
5
6
7
8
9
10
11
12
13
14
15
16
17
18
19
20
21
22
820 The close temporal and spatial eruption of three mafic endmembers at MSH indicates
821 simultaneous tapping of different sources on relatively small scales. LKOT and HFSE-rich
822 basalts derived dominated by decompression melting from at least two distinct fertile
823 lherzolite sources. Both are weakly affected by a subduction component. In contrast, arc-
824 type basaltic andesites likely represent differentiation products of hydrous arc basalt (that
825 did not erupt) generated by flux melting in the mantle. Our data are consistent with a
826 formation of HFSE-rich basalts in the water-poor periphery of the main melting column
827 (potentially tapping an enriched source, Fig. 11, 12a). In those regions water contents and
828 degrees of melting are low(er), leading to higher concentrations of incompatible elements.
829 Weak crustal zones associated with the old fracture system beneath MSH (Weaver et al.
830 1987) likely provide conduits for rapid ascent of individual batches of magma and prevent
831 them from freezing in the crust and hybridization.

23
24
25
26
27
28
29
30
31
32
33
34
35
36
37
38
39
40
41
42
43
44
45
832 The compositional diversity of magmas erupted during the Castle Creek eruptive period of
833 MSH requires repeated injection of mafic magma into the shallow magmatic system. The
834 lack of a *shadow zone* at MSH (i.e., basalts and basaltic andesites erupt through the axial
835 system) that is typically observed at other andesitic to dacitic stratovolcanoes in the
836 Cascades (Hildreth 2007) may be caused by an offset plumbing system, as proposed by
837 seismic tomography (Kiser et al. 2016). Such geometry would facilitate basalt ascent aside
838 from the lower crustal mush zone, before they merge with the upper crustal reservoir,
839 interact with resident dacite, crystallize, and gain their characteristic petrographic
840 appearance (Fig. 12). Conspicuous geochemical trends from the two basaltic endmembers
841 towards basaltic andesite are predominantly caused by assimilation of more evolved calc-
842 alkaline material. Sodic plagioclase cores and rare resorbed mafic minerals in most of the
843 basalts and basaltic andesites form relics of this process.

46 47 48 844 **Acknowledgements**

49
50
51
52
53
54
55
56
57
58
59
60
61
62
63
64
65
845 We thank Lydia Zehnder, Marcel Guillong and Markus Waelle for laboratory assistance
846 during XRF and laser analyses. We appreciate constructive comments from Ben Ellis, Jon
847 Blundy, Sue DeBari, Bill Leeman, Othmar Müntener, and an anonymous reviewer on
848 earlier versions of this manuscript that helped clarify our ideas. This project has been
849 supported by Swiss National Science Foundation grant 200021_146268. Any use of trade,

1
2
3
4
5
6
7
8
9
10
11
12
13
14
15
16
17
18
19
20
21
22
23
24
25
26
27
28
29
30
31
32
33
34
35
36
37
38
39
40
41
42
43
44
45
46
47
48
49
50
51
52
53
54
55
56
57
58
59
60
61
62
63
64
65

850 firm, or product names is for descriptive purposes only and does not imply endorsement by
851 the U.S. Government.

852 **References**

853 Arai S (1994) Characterization of spinel peridotites by olivine-spinel compositional
854 relationships: review and interpretation. *Chem Geol* 113(3-4):191-204

855 Bacon CR (1990) Calc-alkaline, shoshonitic, and primitive tholeiitic lavas from
856 monogenetic volcanoes near Crater Lake, Oregon. *J Petrol* 31(1):135-166

857 Bacon CR, Bruggman PE, Christiansen RL, Clynne MA, Donnelly-Nolan JM, Hildreth W
858 (1997) Primitive magmas at five Cascades volcanic fields: melts from hot, heterogeneous
859 sub-arc mantle. *Can Mineral* 35:397-424

860 Bacon RC, Hirschmann MM (1988) Mg/Mn partitioning as a test for equilibrium between
861 coexisting Fe-Ti oxides. *Am Mineral* 73:57-61

862 Baker MB, Grove TL, Price R (1994) Primitive basalts and andesites from the Mt. Shasta
863 region, N. California: products of varying melt fraction and water content. *Contrib Mineral
864 Petrol* 118(2):111-129

865 Ballhaus C, Berry RF, Green DH (1990) Oxygen fugacity controls in the Earth's upper
866 mantle. *Nature* 348(6300):437-440

867 Bartels KS, Kinzler RJ, Grove TL (1991) High pressure phase relations of primitive high-
868 alumina basalts from Medicine Lake volcano, northern California. *Contrib Mineral Petrol*
869 108(3):253-270

870 Bedrosian PA, Peacock JR, Bowles-Martinez E, Schultz A, Hill GJ (2018) Crustal
871 inheritance and a top-down control on arc magmatism at Mount St. Helens. *Nat Geosci*
872 11:865-870

873 Bindeman IN (2008) Oxygen isotopes in mantle and crustal magmas as revealed by single
874 crystal analysis. *Rev Mineral Geochem* 69:445-478

875 Blatter DL, Sisson TW, Hankins WB (2017) Voluminous arc dacites as amphibole
876 reaction-boundary liquids. *Contrib Mineral Petrol* 172:27(5):1-37

1
2
3
4
5
6
7
8
9
10
11
12
13
14
15
16
17
18
19
20
21
22
23
24
25
26
27
28
29
30
31
32
33
34
35
36
37
38
39
40
41
42
43
44
45
46
47
48
49
50
51
52
53
54
55
56
57
58
59
60
61
62
63
64
65

877 Blundy JD, Cashman KV (2005) Rapid decompression-driven crystallization recorded by
878 melt inclusions from Mount St. Helens volcano. *Geology* 33(10):793–796

879 Blundy JD, Cashman KV, Berlo K (2008) Evolving magma storage conditions beneath
880 Mount St. Helens inferred from chemical variations in melt inclusions from the 1980–1986
881 and current (2004–2006) eruptions. In: Sherrod DR, Scott WE, Stauffer PH (eds) *A*
882 *volcano rekindled: the renewed eruption of Mount St Helens, 2004-2006, USGS Prof Pap*
883 *1750*

884 Borg LE, Clynne MA, Bullen TD (1997) The variable role of slab-derived fluids in the
885 generation of a suite of primitive calc-alkaline lavas from the southernmost cascades,
886 California. *Can Mineral* 35:425-452

887 Cassidy M, Watt S, Talling P, Palmer M, Edmonds M, Jutzeler M, Wall - Palmer D,
888 Manga M, Coussens M, Gernon T (2015) Rapid onset of mafic magmatism facilitated by
889 volcanic edifice collapse. *Geophys Res Lett* 42(12):4778-4785

890 Chiba H, Chacko T, Clayton RN, Goldsmith JR (1989) Oxygen isotope fractionations
891 involving diopside, forsterite, magnetite, and calcite: Application to geothermometry.
892 *Geochim Cosmochim Acta* 53(11):2985-2995

893 Claiborne LL, Miller CF, Flanagan DM, Clynne MA, Wooden JL (2010) Zircon reveals
894 protracted magma storage and recycling beneath Mount St. Helens. *Geology* 38(11):1011-
895 1014

896 Clynne MA, Borg LE (1997) Olivine and chromian spinel in primitive calc-alkaline and
897 tholeiitic lavas from the southernmost Cascade range, California: a reflection of relative
898 fertility of the source. *Can Mineral* 35:453-472

899 Clynne MA, Calvert AT, Wolfe EW, Evarts RC, Fleck RJ, Lanphere MA (2008) The
900 Pleistocene eruptive history of Mount St. Helens, Washington, from 300,000 to 12,800
901 years before present. In: Sherrod DR, Scott WE, Stauffer PH (eds) *A volcano rekindled:*
902 *The renewed eruption of Mount St Helens, 2004-2006, USGS Prof Pap 1750*

903 Conrey RM, Sherrod DR, Hooper PR, Swanson DA (1997) Diverse primitive magmas in
904 the Cascade arc, Northern Oregon and Southern Washington. *Can Mineral* 35(2):367-396

905 Crandell DR (1987) Deposits of pre-1980 pyroclastic flows and lahars from Mount St.
906 Helens volcano, Washington. *USGS Prof Pap* 1444

- 1
2
3
4
5
6
7
8
9
10
11
12
13
14
15
16
17
18
19
20
21
22
23
24
25
26
27
28
29
30
31
32
33
34
35
36
37
38
39
40
41
42
43
44
45
46
47
48
49
50
51
52
53
54
55
56
57
58
59
60
61
62
63
64
65
- 907 Dick HJB, Bullen T (1984) Chromian spinel as a petrogenetic indicator in abyssal and
908 alpine-type peridotites and spatially associated lavas. *Contrib Mineral Petrol* 86(1):54-76
- 909 Dufek J, Bergantz GW (2005) Lower crustal magma genesis and preservation: a stochastic
910 framework for the evaluation of basalt–crust interaction. *J Petrol* 46:2167-2195
- 911 Eiler JM (2001) Oxygen isotope variations of basaltic lavas and upper mantle rocks. *Rev*
912 *Mineral Geochem* 43(1):319-364
- 913 Elkins-Tanton LT, Grove TL, Donnelly-Nolan J (2001) Hot, shallow mantle melting under
914 the Cascades volcanic arc. *Geology* 29(7):631-634
- 915 Fiske RS, Hopson CA, Waters AC (1963) *Geology of Mount Rainier National Park,*
916 *Washington. USGS Prof Pap* 444
- 917 Frost BR (1991) Introduction to oxygen fugacity and its petrologic importance. *Rev*
918 *Mineral Geochem* 25(1):1-9
- 919 Gardner JE, Carey S, Rutherford MJ, Sigurdsson H (1995a) Petrologic diversity in Mount
920 St. Helens dacites during the last 4,000 years: implications for magma mixing. *Contrib*
921 *Mineral Petrol* 119:224-238
- 922 Gardner JE, Rutherford M, Carey S, Sigurdsson H (1995b) Experimental constraints on
923 pre-eruptive water contents and changing magma storage prior to explosive eruptions of
924 Mount St Helens volcano. *Bull Volcanol* 57(1):1-17
- 925 Gill JB (1981) *Orogenic andesites and plate tectonics. Springer-Verlag, Berlin-Heidelberg*
- 926 Grove T, Parman S, Bowring S, Price R, Baker M (2002) The role of an H₂O-rich fluid
927 component in the generation of primitive basaltic andesites and andesites from the Mt.
928 Shasta region, N California. *Contrib Mineral Petrol* 142(4):375-396
- 929 Guillong M, Meier D, Allan M, Heinrich C, Yardley B (2008) SILLs: A MATLAB-based
930 program for the reduction of laser ablation ICP-MS data of homogeneous materials and
931 inclusions. *Mineral Assoc Can Short Course* 40:328-333
- 932 Halliday AN, Fallick AE, Dickin AP, Mackenzie AB, Stephens WE, Hildreth W (1983)
933 The isotopic and chemical evolution of Mount St. Helens. *Earth Planet Sci Lett* 63(2):241-
934 256

1 935 Hansen S, Schmandt B, Levander A, Kiser E, Vidale J, Abers G, Creager K (2016) Seismic
2 936 evidence for a cold serpentinitized mantle wedge beneath Mount St Helens. Nat Comm
3 937 7:13242
4
5
6 938 Hildreth WS (2007) Quaternary magmatism in the Cascades: Geological perspectives.
7 939 USGS Prof Pap 1744
8
9
10 940 Hildreth WS, Fierstein J (1997) Recent eruptions of Mount Adams, Washington Cascades,
11 941 USA. Bull Volcanol 58(6):472-490
12
13
14 942 Hopson CA, Melson WG (1990) Compositional trends and eruptive cycles at Mount St.
15 943 Helens. Geosci Can 17:131-141
16
17
18
19 944 Irvine TN, Baragar WRA (1971) A guide to the chemical classification of the common
20 945 volcanic rocks. Can J Earth Sci 8(5):523-548
21
22
23 946 Jicha BR, Hart GL, Johnson CM, Hildreth W, Beard BL, Shirey SB, Valley JW (2009)
24 947 Isotopic and trace element constraints on the petrogenesis of lavas from the Mount Adams
25 948 volcanic field, Washington. Contrib Mineral Petrol 157(2):189-207
26
27
28
29 949 Karlstrom L, Dufek J, Manga M (2009) Organization of volcanic plumbing through
30 950 magmatic lensing by magma chambers and volcanic loads. J Geophys Res 114:B10204
31
32
33
34 951 Kelemen PB, Hirth G, Shimizu N, Spiegelman M, Dick HJ (1997) A review of melt
35 952 migration processes in the adiabatically upwelling mantle beneath oceanic spreading
36 953 ridges. Phil Trans Roy Soc Math Phys Eng Sci 355(1723):283-318
37
38
39
40 954 Kent AJR, Darr C, Koleszar AM, Salisbury MJ, Cooper KM (2010) Preferential eruption
41 955 of andesitic magmas through recharge filtering. Nat Geosci 3(9):631-636
42
43
44 956 Kinzler RJ, Donnelly-Nolan JM, Grove TL (2000) Late Holocene hydrous mafic
45 957 magmatism at the Paint Pot Crater and Callahan flows, Medicine Lake Volcano, N.
46 958 California and the influence of H₂O in the generation of silicic magmas. Contrib Mineral
47 959 Petrol 138(1):1-16
48
49
50
51
52 960 Kiser E, Levander A, Zelt C, Schmandt B, Hansen S (2018) Focusing of melt near the top
53 961 of the Mount St. Helens (USA) magma reservoir and its relationship to major volcanic
54 962 eruptions. Geology 46(9):775-778
55
56
57
58
59
60
61
62
63
64
65

1 963 Kiser E, Palomeras I, Levander A, Zelt C, Harder S, Schmandt B, Hansen S, Creager K,
2 964 Ulberg C (2016) Magma reservoirs from the upper crust to the Moho inferred from high-
3 965 resolution Vp and Vs models beneath Mount St. Helens, Washington State, USA. *Geology*
4 966 44(6):411-414

5
6
7 967 Larsen LM, Pedersen AK (2000) Processes in high-Mg, high-T magmas: evidence from
8 968 olivine, chromite and glass in Palaeogene picrites from West Greenland. *J Petrol*
9 969 41(7):1071-1098

10
11
12
13 970 Le Bas MJ, Le Maitre RW, Streckeisen A, Zanettin B, Rocks ISotSoI (1986) A chemical
14 971 classification of volcanic rocks based on the total alkali-silica diagram. *J Petrol* 27(3):745-
15 972 750

16
17
18
19 973 Le Voyer M, Rose-Koga EF, Shimizu N, Grove TL, Schiano P (2010) Two contrasting
20 974 H₂O-rich components in primary melt inclusions from Mount Shasta. *J Petrol* 51(7):1571-
21 975 1595

22
23
24
25 976 Leeman WP, Lewis JF, Evarts RC, Conrey RM, Streck MJ (2005) Petrologic constraints on
26 977 the thermal structure of the Cascades arc. *J Volcanol Geotherm Res* 140(1-3):67-105

27
28
29
30 978 Leeman WP, Smith DR (2018) The role of magma mixing, identification of mafic magma
31 979 inputs, and structure of the underlying magmatic system at Mount St. Helens. *Am Mineral*,
32 980 in press

33
34
35
36 981 Leeman WP, Smith DR, Hildreth W, Palacz Z, Rogers N (1990) Compositional diversity of
37 982 Late Cenozoic basalts in a transect across the southern Washington Cascades: Implications
38 983 for subduction zone magmatism. *J Geophys Res* 95(B12):19561-19582

39
40
41
42 984 Leeman WP, Tonarini S, Chan LH, Borg LE (2004) Boron and lithium isotopic variations
43 985 in a hot subduction zone—the southern Washington Cascades. *Chem Geol* 212(1):101-124

44
45
46
47 986 Martin-Short R, Allen RM (2013) Mantle Flow Geometry Through the Segmented Juan de
48 987 Fuca Plate. *Berkeley Seismological Laboratory*:16

49
50
51 988 Maurel C, Maurel P (1982) Etude experimentale de l'équilibre Fe²⁺-Fe³⁺ dans les
52 989 spinelles chromifères et les liquides silicates basiques coexistants à 1 atm. *CR Acad Sci*
53 990 Paris 285:209-215

- 1
2
3
4
5
6
7
8
9
10
11
12
13
14
15
16
17
18
19
20
21
22
23
24
25
26
27
28
29
30
31
32
33
34
35
36
37
38
39
40
41
42
43
44
45
46
47
48
49
50
51
52
53
54
55
56
57
58
59
60
61
62
63
64
65
- 991 McCrory PA, Blair JL, Waldhauser F, Oppenheimer DH (2012) Juan de Fuca slab
992 geometry and its relation to Wadati - Benioff zone seismicity. *J Geophys Res [Solid Earth]*
993 117:B9
- 994 Miyashiro A (1974) Volcanic rock series in island arcs and active continental margins. *Am*
995 *J Sci* 274:321-355
- 996 Moore NE, DeBari SM (2012) Mafic magmas from Mount Baker in the northern Cascade
997 arc, Washington: probes into mantle and crustal processes. *Contrib Mineral Petrol*
998 163(3):521-546
- 999 Muffler L, Clynne M, Calvert A, Champion D (2011) Diverse, discrete, mantle-derived
1000 batches of basalt erupted along a short normal fault zone: The Poison Lake chain,
1001 southernmost Cascades. *Geol Soc Am Bull* 123:2177-2200
- 1002 Mullen EK, McCallum IS (2014) Origin of basalts in a hot subduction setting: petrological
1003 and geochemical insights from Mt. Baker, Northern Cascade Arc. *J Petrol* 55(2):241-281
- 1004 Mullen EK, Weis D, Marsh NB, Martindale M (2017) Primitive arc magma diversity: New
1005 geochemical insights in the Cascade Arc. *Chem Geol* 448:43-70
- 1006 Mullineaux DR (1996) Pre-1980 tephra-fall deposits erupted from Mount St Helens,
1007 Washington. USGS Prof Pap 1563
- 1008 Pallister JS, Clynne MA, Wright HM, Van Eaton AR, Vallance JW, Sherrod DR, Kokelaar
1009 BP (2017) Field-trip guide to Mount St. Helens, Washington-An overview of the eruptive
1010 history and petrology, tephra deposits, 1980 pyroclastic density current deposits, and the
1011 crater. USGS Sci Inv Rep 2917-5022-D
- 1012 Pallister JS, Hoblitt RP, Crandell DR, Mullineaux DR (1992) Mount St. Helens a decade
1013 after the 1980 eruptions: magmatic models, chemical cycles, and a revised hazards
1014 assessment. *Bull Volcanol* 54(2):126-146
- 1015 Pallister JS, Thornber CR, Cashman KV, Clynne MA, Lowers HA, Mandeville CW,
1016 Brownfield IK, Meeker GP (2008) Petrology of the 2004-2006 Mount St. Helens lava
1017 dome-implications for magmatic plumbing and eruption triggering. In: Sherrod DR, Scott
1018 WE, Stauffer PH (eds) *A volcano rekindled: the renewed eruption of Mount St Helens,*
1019 *2004-2006, USGS Prof Pap 1750*

- 1020 Parsons T, Wells RE, Fisher MA, Flueh E, ten Brink US (1999) Three-dimensional
1021 velocity structure of Siletzia and other accreted terranes in the Cascadia forearc of
1022 Washington. *J Geophys Res [Solid Earth]* 104(B8):18015-18039
- 1023 PetDB (2015) Petrological Database of the Ocean Floor: <http://www.earthchem.org/petdb>.
1024 Accessed July 2015
- 1025 Pin C, Briot D, Bassin C, Poitrasson F (1994) Concomitant separation of strontium and
1026 samarium-neodymium for isotopic analysis in silicate samples, based on specific extraction
1027 chromatography. *Anal Chim Acta* 298(2):209-217
- 1028 Putirka K (2008) Thermometers and barometers for volcanic systems. *Rev Mineral*
1029 *Geochem* 69:61-120
- 1030 Putirka KD (2005) Igneous thermometers and barometers based on plagioclase + liquid
1031 equilibria: Tests of some existing models and new calibrations. *Am Mineral* 90:336-346
- 1032 Rea J, Wallace PJ, Clynne MA (2012) Pre-eruptive volatile content of mafic magma from
1033 the 2.0-1.7 ka Castle Creek eruptive period, Mount St. Helens. In: AGU Fall Meeting 2012
1034 Abstracts, vol., pp abstract no. V53C-2853
- 1035 Reiners PW, Hammond PE, McKenna JM, Duncan RA (2000) Young basalts of the central
1036 Washington Cascades, flux melting of the mantle, and trace element signatures of primary
1037 arc magmas. *Contrib Mineral Petrol* 138(3):249-264
- 1038 Rose EF, Shimizu N, Layne GD, Grove TL (2001) Melt production beneath Mt. Shasta
1039 from boron data in primitive melt inclusions. *Science* 293(5528):281-283
- 1040 Rowe MC, Kent AJ, Nielsen RL (2009) Subduction influence on oxygen fugacity and trace
1041 and volatile elements in basalts across the Cascade Volcanic Arc. *J Petrol* 50(1):61-91
- 1042 Ruscitto D, Wallace P, Johnson E, Kent A, Bindeman I (2010) Volatile contents of mafic
1043 magmas from cinder cones in the Central Oregon High Cascades: Implications for magma
1044 formation and mantle conditions in a hot arc. *Earth Planet Sci Lett* 298(1):153-161
- 1045 Sas M, Debari SM, Clynne MA, Rusk BG (2017) Using mineral geochemistry to decipher
1046 slab, mantle, and crustal input in the generation of high-Mg andesites and basaltic
1047 andesites from the northern Cascade Arc. *Am Mineral* 102(5):948-965

1048 Sauerzapf U, Lattard D, Burchard M, Engelmann R (2008) The Titanomagnetite–Ilmenite
1 1049 Equilibrium: New Experimental Data and Thermo-oxybarometric Application to the
2
3 1050 Crystallization of Basic to Intermediate Rocks. *J Petrol* 49(6):1161-1185
4
5
6 1051 Scandone R, Malone SD (1985) Magma supply, magma discharge and readjustment of the
7 1052 feeding system of Mount St. Helens during 1980. *J Volcanol Geotherm Res* 23(3-4):239-
8 1053 262
9
10
11 1054 Schmandt B, Humphreys E (2010) Complex subduction and small-scale convection
12 1055 revealed by body-wave tomography of the western United States upper mantle. *Earth*
13 1056 *Planet Sci Lett* 297(3):435-445
14
15
16
17 1057 Schmidt ME, Grunder AL, Rowe MC (2008) Segmentation of the Cascade Arc as indicated
18 1058 by Sr and Nd isotopic variation among diverse primitive basalts. *Earth Planet Sci Lett*
19 1059 266(1):166-181
20
21
22
23 1060 Schmidt MW, Poli S (1998) Experimentally based water budgets for dehydrating slabs and
24 1061 consequences for arc magma generation. *Earth Planet Sci Lett* 163(1-4):361-379
25
26
27
28 1062 Scott W, Gardner C, Sherrod D, Tilling R, Lanphere M, Conrey R (1997) Geologic history
29 1063 of Mount Hood Volcano, Oregon: A field-trip guidebook. USGS Open-File Rep 97-263
30
31
32 1064 Sisson TW, Grove TL (1993) Experimental investigations of the role of H₂O in calc-
33 1065 alkaline differentiation and subduction zone magmatism. *Contrib Mineral Petrol*
34 1066 113(2):143-166
35
36
37
38 1067 Sisson TW, Layne GD (1993) H₂O in basalt and basaltic andesite glass inclusions from
39 1068 four subduction-related volcanoes. *Earth Planet Sci Lett* 117(3):619-635
40
41
42
43 1069 Sisson TW, Salters VJM, Larson PB (2014) Petrogenesis of Mount Rainier andesite:
44 1070 Magma flux and geologic controls on the contrasting differentiation styles at
45 1071 stratovolcanoes of the southern Washington Cascades. *Geol Soc Am Bull* 126(1-2):122-
46 1072 144
47
48
49
50
51 1073 Smith DR (1984) The petrology and geochemistry of High Cascade Volcanics in Southern
52 1074 Washington: Mount St. Helens Volcano and the Indian Heaven basalt field. Rice
53 1075 University

1 1076 Smith DR, Leeman WP (1993) The origin of Mount St. Helens andesites. *J Volcanol*
2 1077 *Geotherm Res* 55(3-4):271-303
3
4 1078 Smith DR, Leeman WP (2005) Chromian spinel–olivine phase chemistry and the origin of
5 1079 primitive basalts of the southern Washington Cascades. *J Volcanol Geotherm Res* 140(1–
6 1080 3):49-66
7
8
9
10 1081 Spiegelman M, Kelemen PB (2003) Extreme chemical variability as a consequence of
11 1082 channelized melt transport. *Geochem Geophys Geosyst* 4(7):7
12
13
14 1083 Streck MJ, Leeman WP (2018) Petrology of “Mt. Shasta” high-magnesian andesite
15 1084 (HMA): A product of multi-stage crustal assembly. *American Mineralogist: Journal of*
16 1085 *Earth and Planetary Materials* 103(2):216-240
17
18
19
20
21 1086 Sun SS, McDonough WF (1989) Chemical and isotopic systematics of oceanic basalts:
22 1087 implications for mantle composition and processes. *Geol Soc Spec Pub* 42:313-345
23
24
25 1088 Walowski KJ, Wallace PJ, Clyne MA, Rasmussen DJ, Weis D (2016) Slab melting and
26 1089 magma formation beneath the southern Cascade arc. *Earth Planet Sci Lett* 446:100-112
27
28
29 1090 Wan Z, Coogan LA, Canil D (2008) Experimental calibration of aluminum partitioning
30 1091 between olivine and spinel as a geothermometer. *Am Mineral* 93(7):1142-1147
31
32
33
34 1092 Weaver CS, Grant WC, Shemeta JE (1987) Local crustal extension at Mount St. Helens,
35 1093 Washington. *J Geophys Res* 92(B10):10170-10178
36
37
38 1094 Wells R, Bukry D, Friedman R, Pyle D, Duncan R, Haeussler P, Wooden J (2014)
39 1095 Geologic history of Siletzia, a large igneous province in the Oregon and Washington Coast
40 1096 Range: Correlation to the geomagnetic polarity time scale and implications for a long-lived
41 1097 Yellowstone hotspot. *Geosphere* 10(4):692-719
42
43
44
45 1098 Wells RE, Weaver CS, Blakely RJ (1998) Fore-arc migration in Cascadia and its
46 1099 neotectonic significance. *Geology* 26(8):759-762
47
48
49
50 1100 Williams DA, Kadel SD, Greeley R, Leshner CM, Clyne MA (2004) Erosion by flowing
51 1101 lava: geochemical evidence in the Cave Basalt, Mount St. Helens, Washington. *Bull*
52 1102 *Volcanol* 66(2):168-181
53
54
55
56 1103

- 1
- 2
- 3
- 4
- 5
- 6
- 7
- 8
- 9
- 10
- 11
- 12
- 13
- 14
- 15
- 16
- 17
- 18
- 19
- 20
- 21
- 22
- 23
- 24
- 25
- 26
- 27
- 28
- 29
- 30
- 31
- 32
- 33
- 34
- 35
- 36
- 37
- 38
- 39
- 40
- 41
- 42
- 43
- 44
- 45
- 46
- 47
- 48
- 49
- 50
- 51
- 52
- 53
- 54
- 55
- 56
- 57
- 58
- 59
- 60
- 61
- 62
- 63
- 64
- 65

1105 **Fig. 1** Shaded relief map of the Mount St. Helens area showing sample localities of Castle
1106 Creek rocks. Symbols and colors for different units are explained in Table 1. Black lines
1107 show major tectonic boundaries as discussed by Weaver et al. (1987) including the NNW-
1108 striking St. Helens seismic zone and a pre-Quaternary NE-striking set of fractures. The
1109 inset map indicates the position of Mount St. Helens about 50 km west of the main
1110 volcanic axis of the Cascade arc.

1111 **Fig. 2** Major element variations vs. SiO₂ of volcanic rocks from the Castle Creek period of
1112 Mount St. Helens. Each color refers to a single mafic unit (same as in Table 1). Symbols
1113 outlined in black indicate samples from this study; others compile literature and previously
1114 unpublished data (Appendix A4). All whole-rock data is normalized to 100 % with FeO*
1115 recalculated as FeO and Fe₂O₃ assuming Fe³⁺/ΣFe = 0.2, except for the LKOT endmember
1116 (Cave Basalt, Fe³⁺/ΣFe = 0.15). (a) Total alkali vs. silica (TAS) diagram after Le Bas et al.
1117 (1986) showing the classification of Castle Creek rocks. The dashed line divides alkaline
1118 and subalkaline rocks (Irvine and Baragar 1971). (b) K₂O vs. SiO₂. Dashed lines separate
1119 the fields of low-K, medium-K, and high-K after Gill (1981). (c) FeO*/MgO. Fields for
1120 tholeiitic and calc-alkalic rocks are shown after Miyashiro (1974).

1121 **Fig. 3** Major element variations vs. MgO. Symbols as in Table 1. Shaded fields show
1122 compositions of different types of primitive basalts across the southern Washington
1123 Cascades taken from Leeman et al. (2005) and references therein: calc-alkaline basalts
1124 (CAB), low-K olivine tholeiites (LKOT), nepheline-normative ocean island-type (ALK)
1125 basalts, and hypersthene-normative ocean island-type basalts (OIB).

1126 **Fig. 4** Trace element variations in Castle Creek rocks. Most incompatible trace elements
1127 form trends from LKOT and HFSE-rich basalt endmembers towards basaltic andesite as
1128 shown by most major elements. Symbols and fields as in Fig. 3. Some more compatible
1129 elements occur in the same abundances in both series.

1130 **Fig. 5** Rare earth elements (left) and incompatible trace elements (right) normalized to
1131 chondrite and primitive mantle (Sun and McDonough 1989), respectively, in LKOT,
1132 HFSE-rich basalts, and arc-type basaltic andesites. Compositions of Castle Creek dacites,
1133 Cascade LKOT, HFSE-rich basalts and CAB (colored fields, Mullen et al. 2017), and

1134 normal mid ocean ridge basalts (N-MORB), enriched (E-) MORB and ocean island basalts
1135 (OIB) (Sun and McDonough 1989) are shown for comparison.

1136 **Fig. 6** Isotopic compositions of Castle Creek period rocks spanning basaltic to dacitic
1137 compositions. Isotope data from Halliday et al. (1983) and Leeman et al. (1990) is shown
1138 for comparison. (a) $^{143}\text{Nd}/^{144}\text{Nd}$ vs. $^{87}\text{Sr}/^{86}\text{Sr}$. The grey field indicates compositions of
1139 primitive Cascade arc rocks (Mullen and McCallum 2014 and references therein). The
1140 inset shows the samples in a broader isotopic framework including bulk silicate earth
1141 (BSE), depleted mantle (DM), high ' μ ' = $^{238}\text{U}/^{204}\text{Pb}$ (HIMU), and enriched mantle 1 and 2
1142 (EMI and EMII). (b) $^{87}\text{Sr}/^{86}\text{Sr}$ vs. SiO_2 , (c) $\delta^{18}\text{O}$ vs. $^{87}\text{Sr}/^{86}\text{Sr}$, and (d) $\delta^{18}\text{O}$ vs. SiO_2 of
1143 whole-rocks and plagioclase and olivine separates. Fields for mid ocean ridge basalts
1144 (MORB) and the array of $\delta^{18}\text{O}$ during closed system differentiation are taken from
1145 Bindeman (2008).

1146 **Fig. 7** Backscattered electron images showing (a) a glomerocrystic aggregate with weakly
1147 normally zoned plagioclase and olivine from the Cave Basalt (LKOT endmember), (b-d)
1148 reversely and complexly zoned plagioclase crystals from HFSE-rich basalts and basaltic
1149 andesites with sodic cores that are partly or completely resorbed and recrystallized. Some
1150 show alternating zones of internal normal zonation. Rims are normally zoned. (e) olivine
1151 crystals with a thin Fa-rich rim and chromian spinel inclusions from HFSE-rich basalt, (f)
1152 olivine crystal with spinel inclusions rimmed by orthopyroxene from an arc-type basaltic
1153 andesite.

1154 **Fig. 8** Histograms of anorthite (An) content in plagioclase comparing core and rim
1155 compositions of normally and reversely/complexly zoned crystals in different Castle Creek
1156 units. Units are shown in stratigraphic order from lower left to upper right. Normally
1157 zoned crystal cores overlap with rims of reversely zoned crystals.

1158 **Fig. 9** Compositional variations in olivine and chromian spinel inclusions in different
1159 Castle Creek units. (a) Rhodes diagram showing the forsterite (Fo) content of the olivine
1160 vs. Mg# in whole-rock ($\text{Mg\#} = \text{Mg}/(\text{Mg}+\text{Fe}^{2+})$, calculated on a molar basis assuming
1161 $\text{Fe}^{3+}/\Sigma\text{Fe} = 0.15$ for the Cave Basalt and 0.2 for all other mafic units). The equilibrium line
1162 refers to a $K_D(\text{Fe-Mg})^{\text{ol-liq}}$ of 0.3 ± 0.03 (Putirka 2008). Filled symbols indicate crystal cores,
1163 unfilled symbols crystal rims. Sparsely occurring type 2 and 3 olivines in the pre-Cave

1164 Basalt and the basalt of the south flank are shown as crossed squares. (b) Cr# (Cr# =
1165 Cr/(Cr+Al)) vs. Fo content of contiguous olivine-spinel pairs. The arrow in the olivine
1166 spinel mantle array (OSMA, Arai 1994) indicates increasing refractoriness of the mantle
1167 source and/or increasing degrees of partial melting. Colored fields show spinel
1168 compositions of southern Washington LKOT (open diamonds), HFSE-rich basalts (open
1169 triangles), and CAB (black points) of Smith and Leeman (2005). (c) Spinel Cr# vs. Mg#.

1170 **Fig. 10** (a) Oxygen fugacity (fO_2) vs. temperature (T) calculated from olivine-spinel pairs
1171 of different units (Ballhaus et al. 1990; Wan et al. 2008). Spinel with Mg# <0.6 is shown in
1172 opacity. Quartz-fayalite-magnetite (QFM) buffer curves are indicated for QFM (continuous
1173 line) and QFM+2 (dashed line) (Frost 1991). Magmatic temperatures of the two basalt
1174 groups and their endmembers determined by different thermometers by Leeman and Smith
1175 (2018) are shown for comparison. (b) Ca-Na exchange between plagioclase and liquid.
1176 Ca/Na plagioclase is shown for the most calcic plagioclase composition in cores of
1177 normally zoned crystals (filled symbols) and in outer zones of reversely zoned crystals
1178 (empty symbols) of different units; outliers in two units are displayed in opacity. Ca/Na
1179 liquid is taken from molar whole-rock (wr) compositions. An arrow illustrates the effect of
1180 dacite assimilation. Lines indicate experimental partition coefficients (K_D) from Sisson and
1181 Grove (1993) referring to 2, 4, and 6 wt% H₂O, respectively.

1182 **Fig. 11** (a) Ba/Zr vs. Nb/Zr, (b) Ba/Nb vs. Nb, (c) Zr/Nb vs. La/Yb, (d) Zr/Nb vs. Dy/Yb.
1183 Symbols and colors as in Fig. 3. Note that Zr/Nb and La/Yb are plotted on log scales. The
1184 grey field in (a) indicates the compositional range of oceanic basalts from Leeman et al.
1185 (1990). Compositions from N-MORB, E-MORB and OIB after Sun and McDonough
1186 (1989) and the East Pacific Rise (EPR) (PetDB 2015) are shown for comparison.

1187 **Fig. 12** (a) Perspective view of the proposed magmatic plumbing system of MSH with the
1188 three basalt types derived from different mantle sources. Hydrous arc basalts are generated
1189 by flux melting in the mantle wedge, whereas HFSE-rich basalt derived from the (water-
1190 poor) periphery of the main melting column, potentially tapping an enriched source. LKOT
1191 derived by decompression melting from a fertile lherzolite source in the uppermost mantle.
1192 Note that the spatial distribution of mantle sources is schematic and remains speculative.
1193 Arc basalts predominantly feed the lower crustal mush zone, while peripheral LKOT and
1194 HFSE-rich basalts bypass the main lower crustal plumbing system. Crust and mantle

1195 geometry is based on Parsons et al. (1999) and McCrory et al. (2012). The positions of the
1196 magma reservoirs are inferred from seismic low velocity zones (Kiser et al. 2016). The
1197 outline of the upper crustal magma reservoir is taken from Scandone and Malone (1985)
1198 and Pallister et al. (2008). The serpentinized mantle wedge and magma transport into the
1199 wedge from further east is shown as suggested by Hansen et al. (2016). (b) Schematic
1200 cross-section section through the upper crustal magma reservoir illustrating the
1201 entrainment of antecrystic material into the HFSE-rich north flank basalt and (c) the
1202 entrainment of cognate crystal mush into the Cave Basalt (LKOT) after the pathway was
1203 cleaned by preceding basalts. The upper crustal mush is pictured as plagioclase (white,
1204 striped), amphibole (brown), pyroxene (green), oxides (black), and melt (light grey).

Figure 1

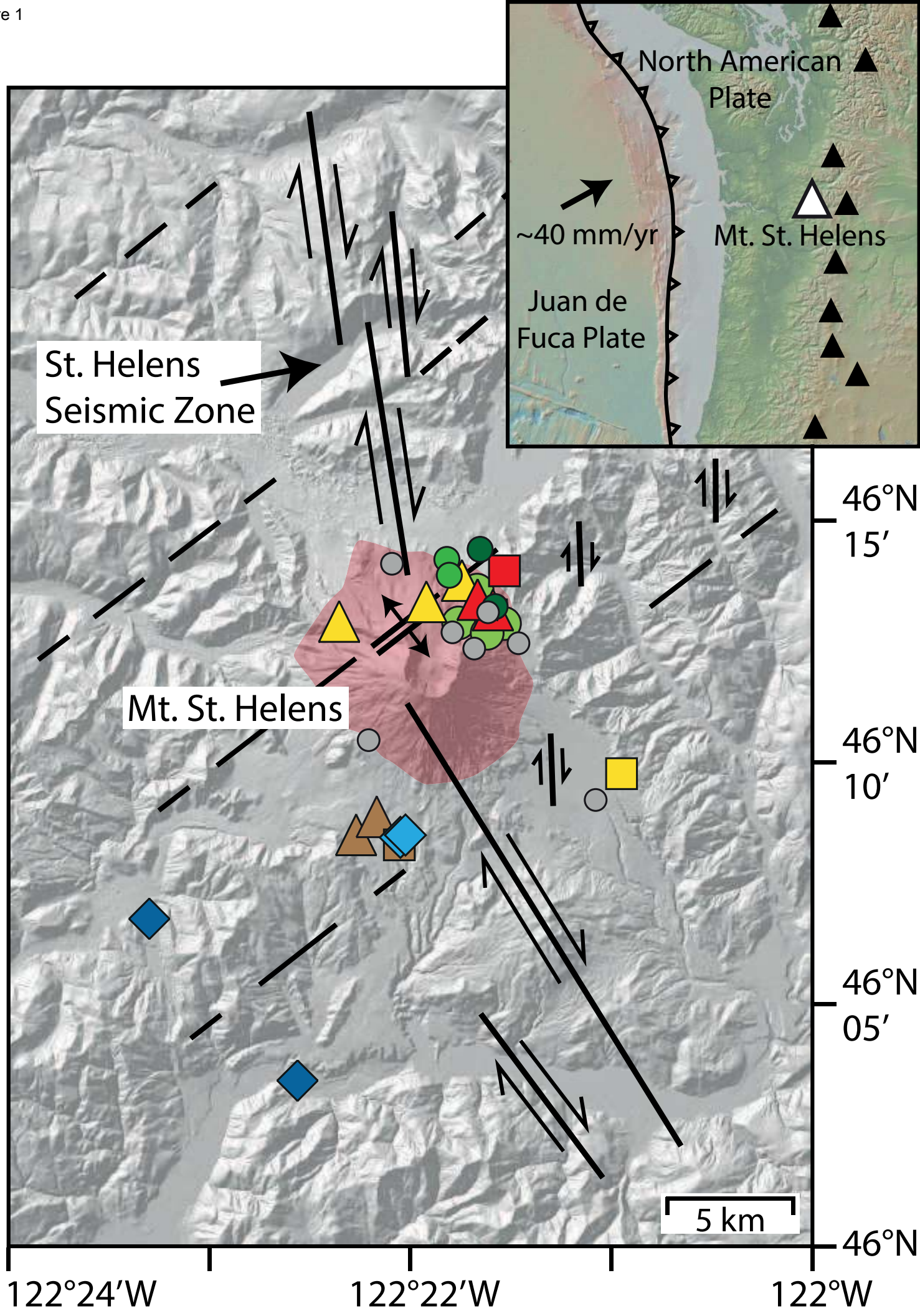
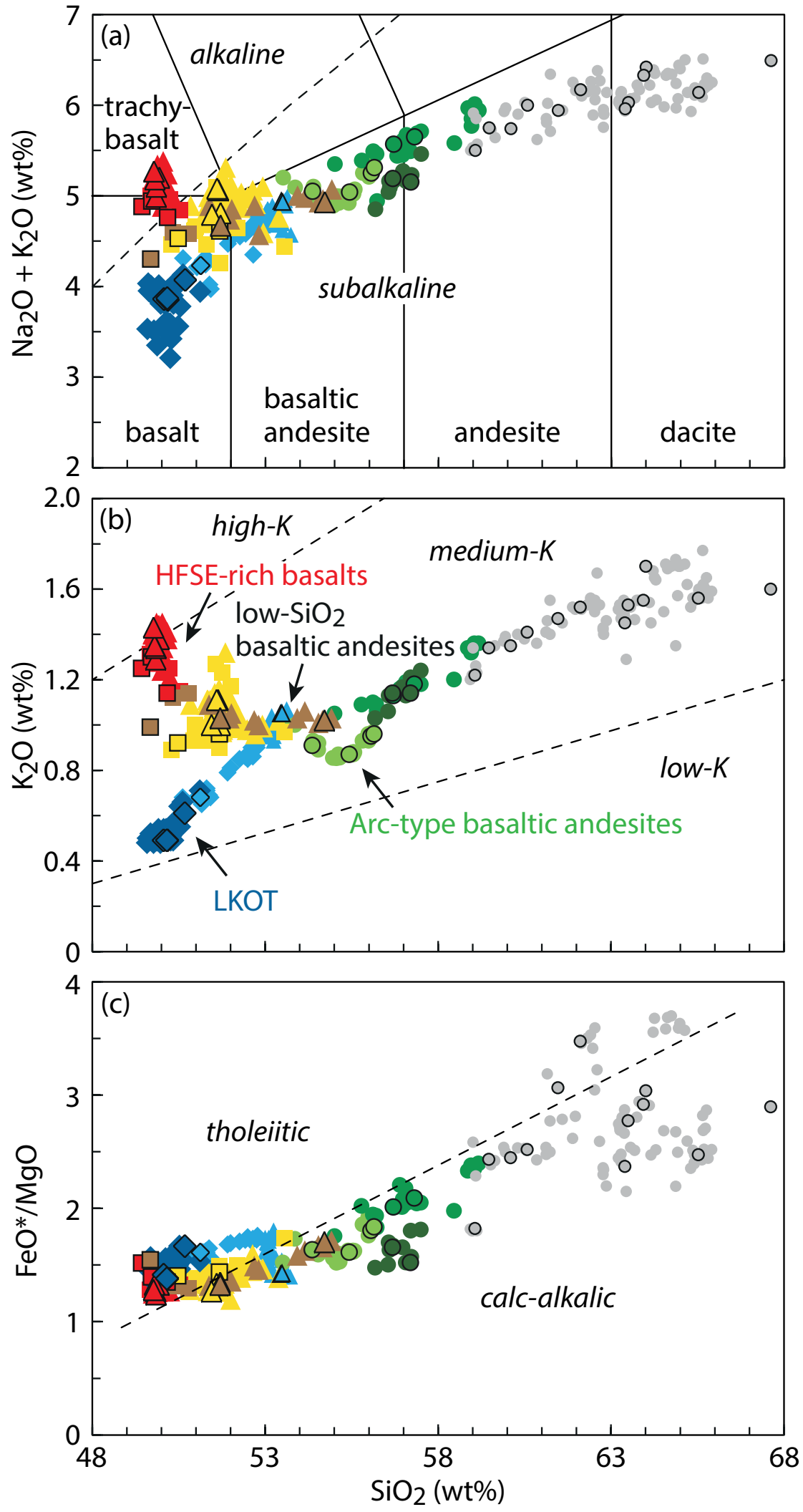


Figure 2



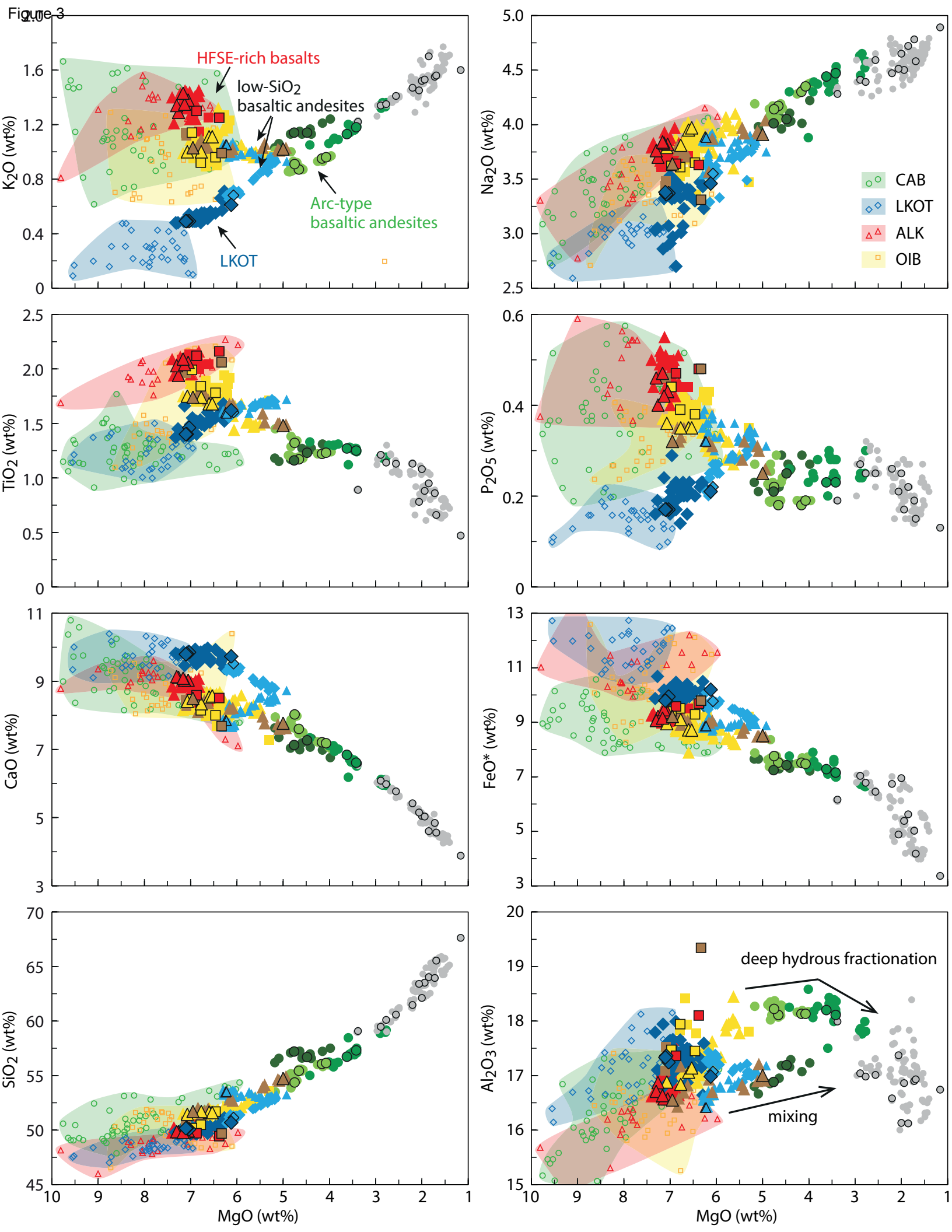


Figure 4

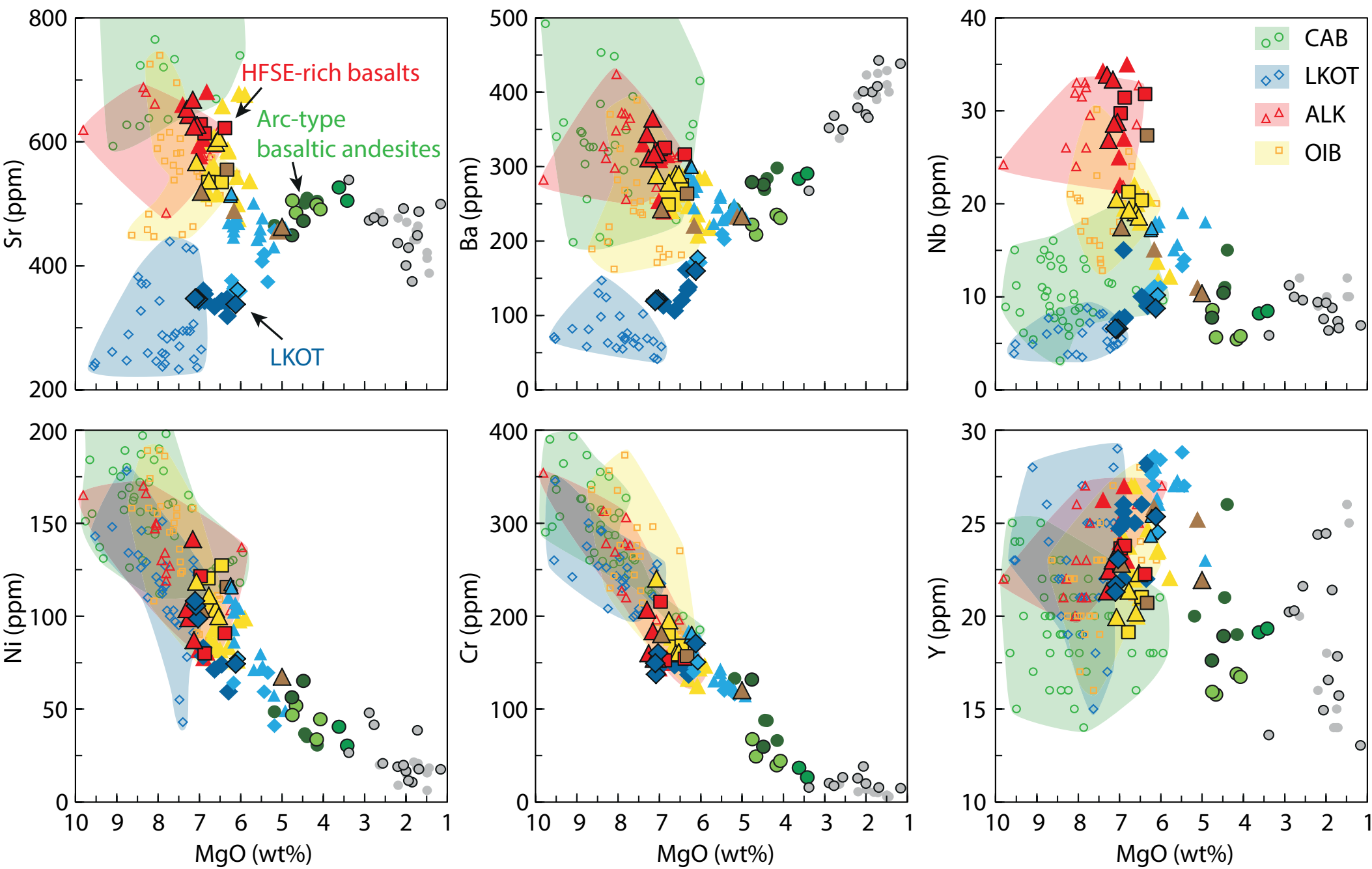


Figure 5

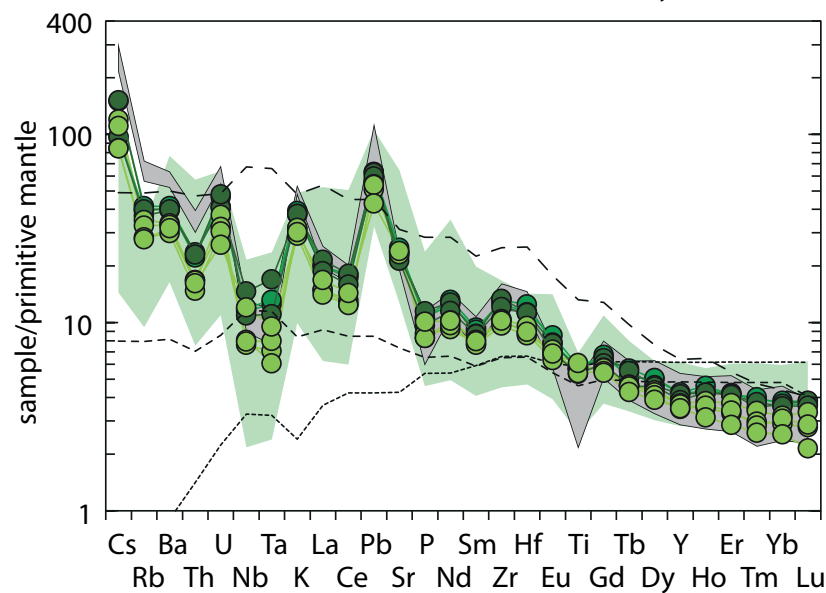
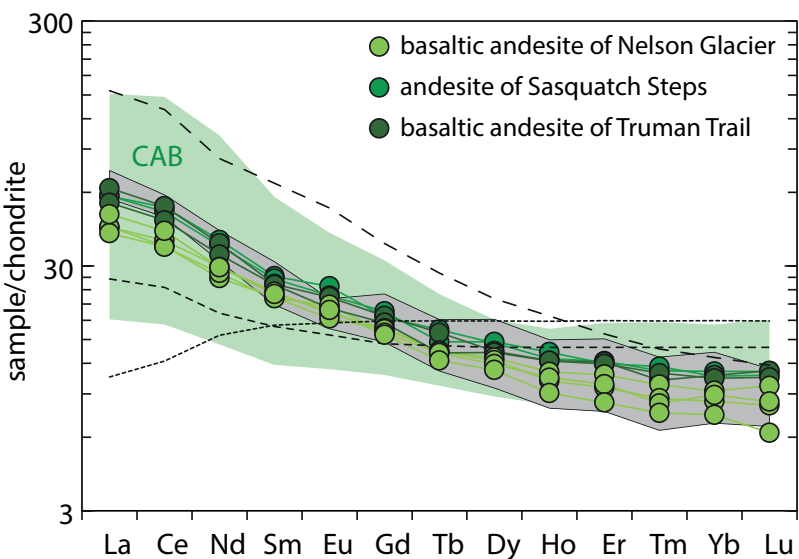
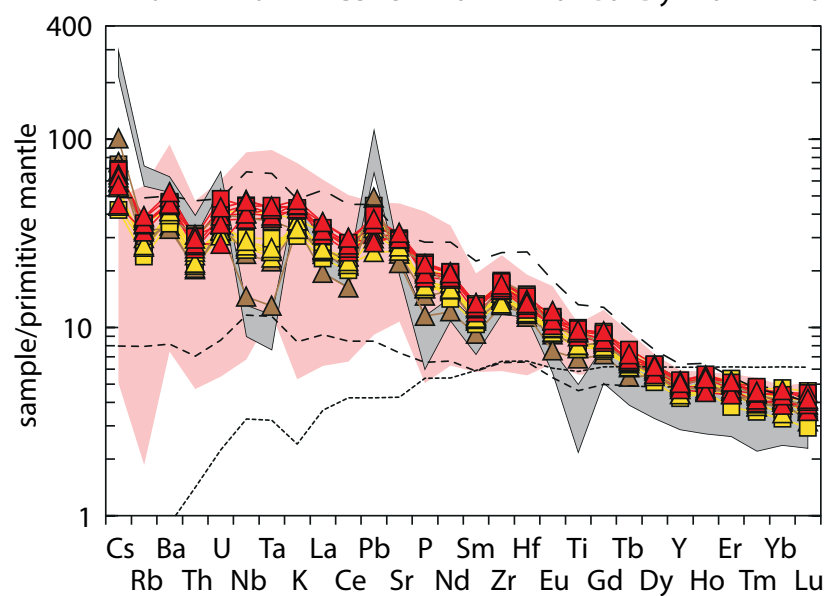
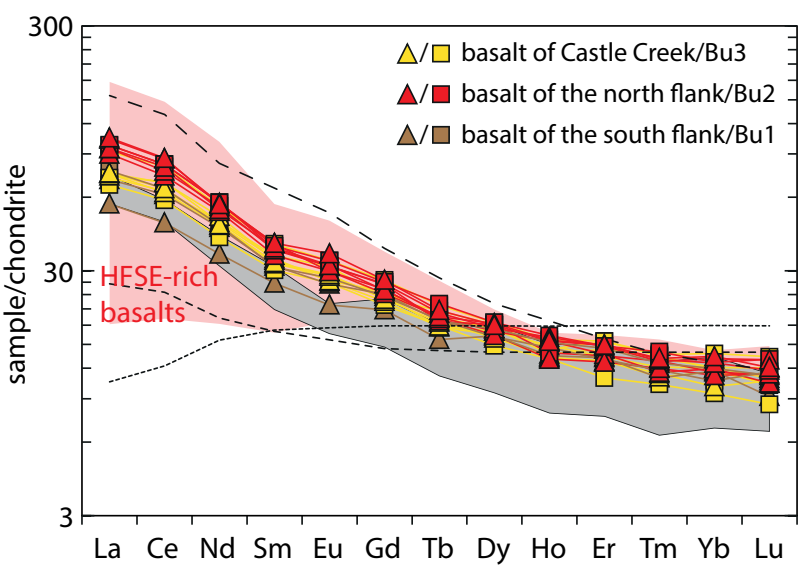
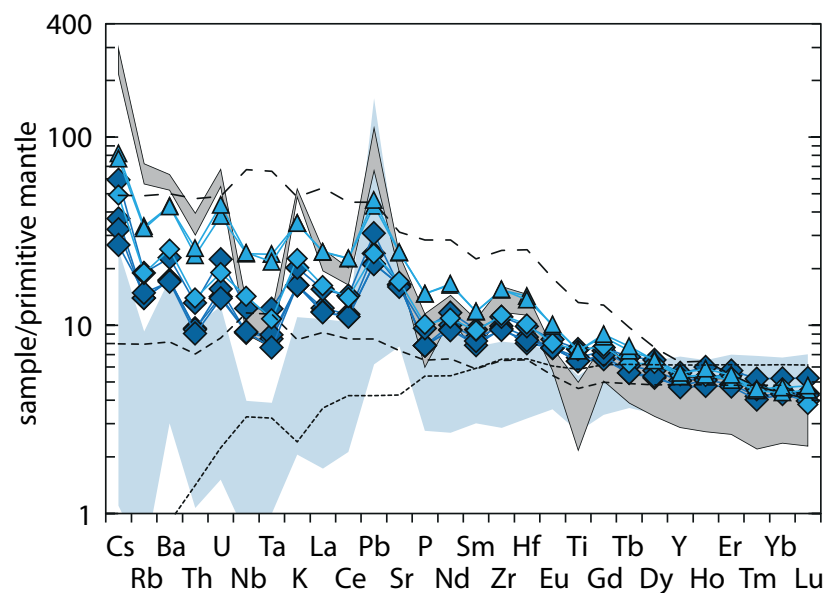
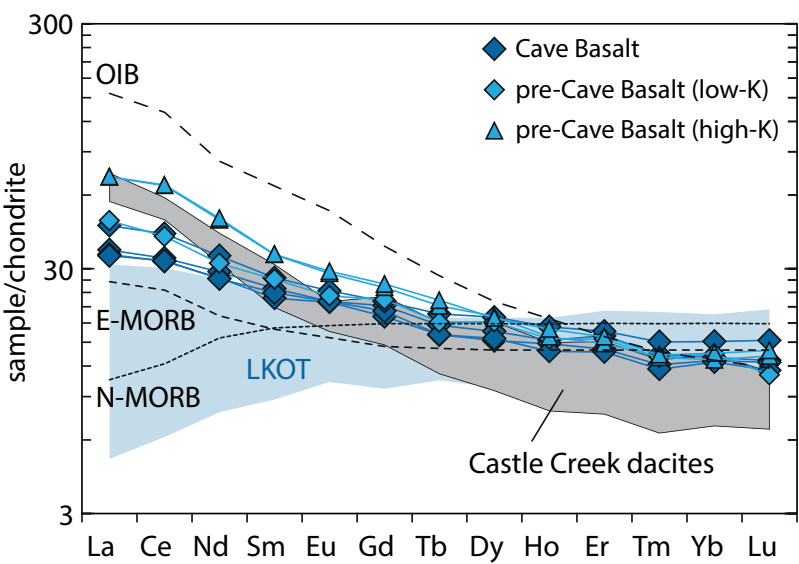


Figure 6

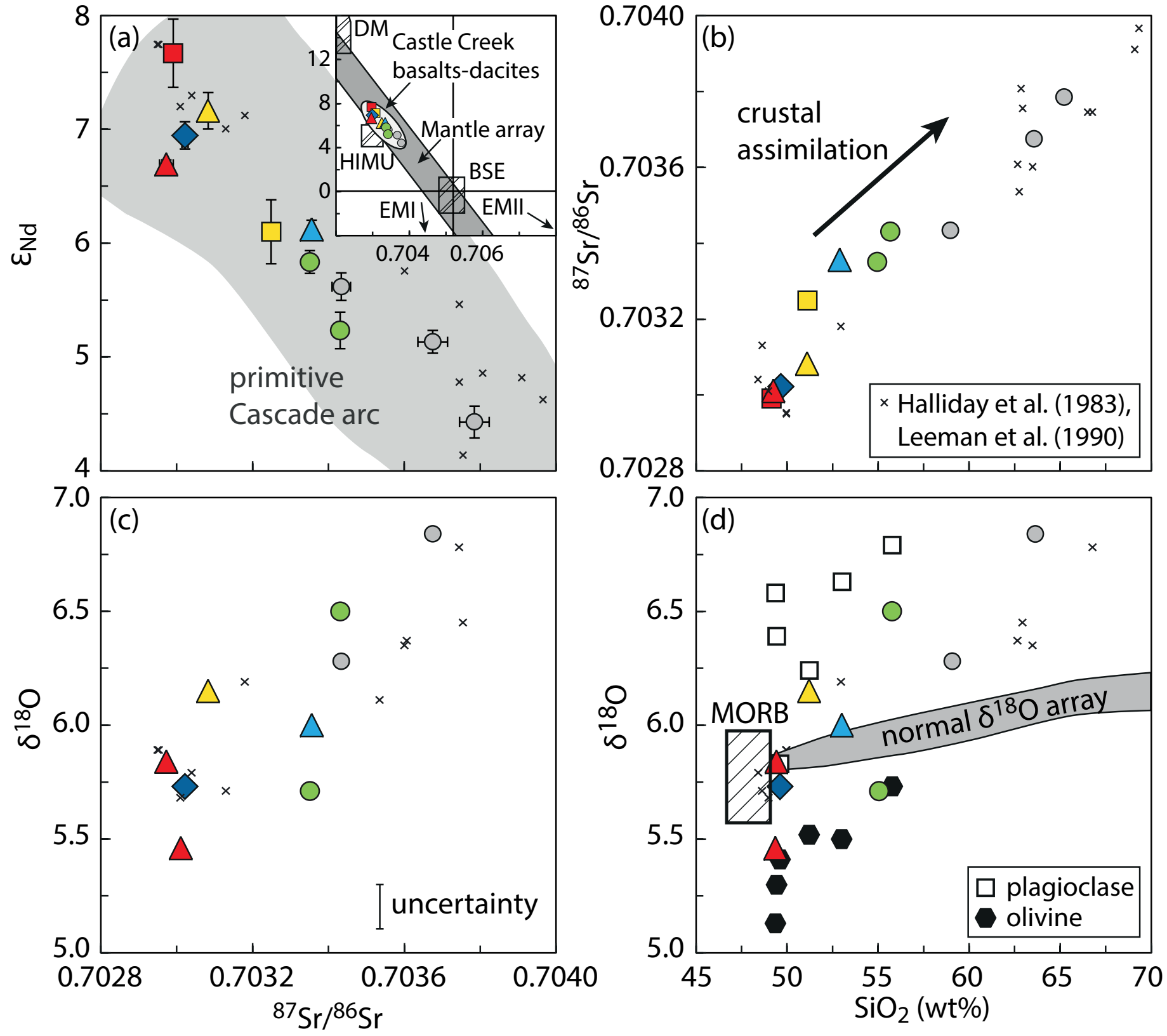


Figure 7

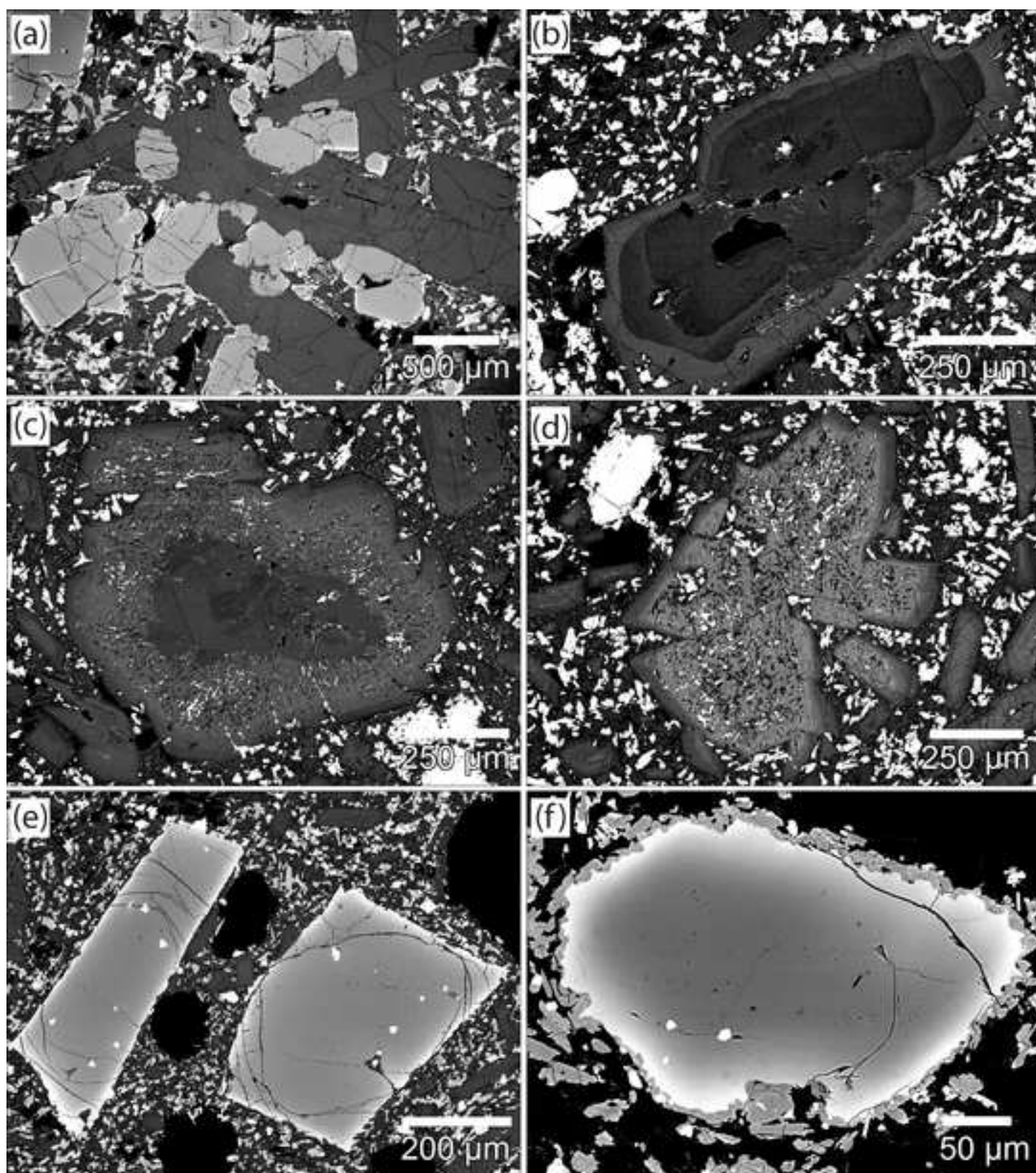


Figure 9

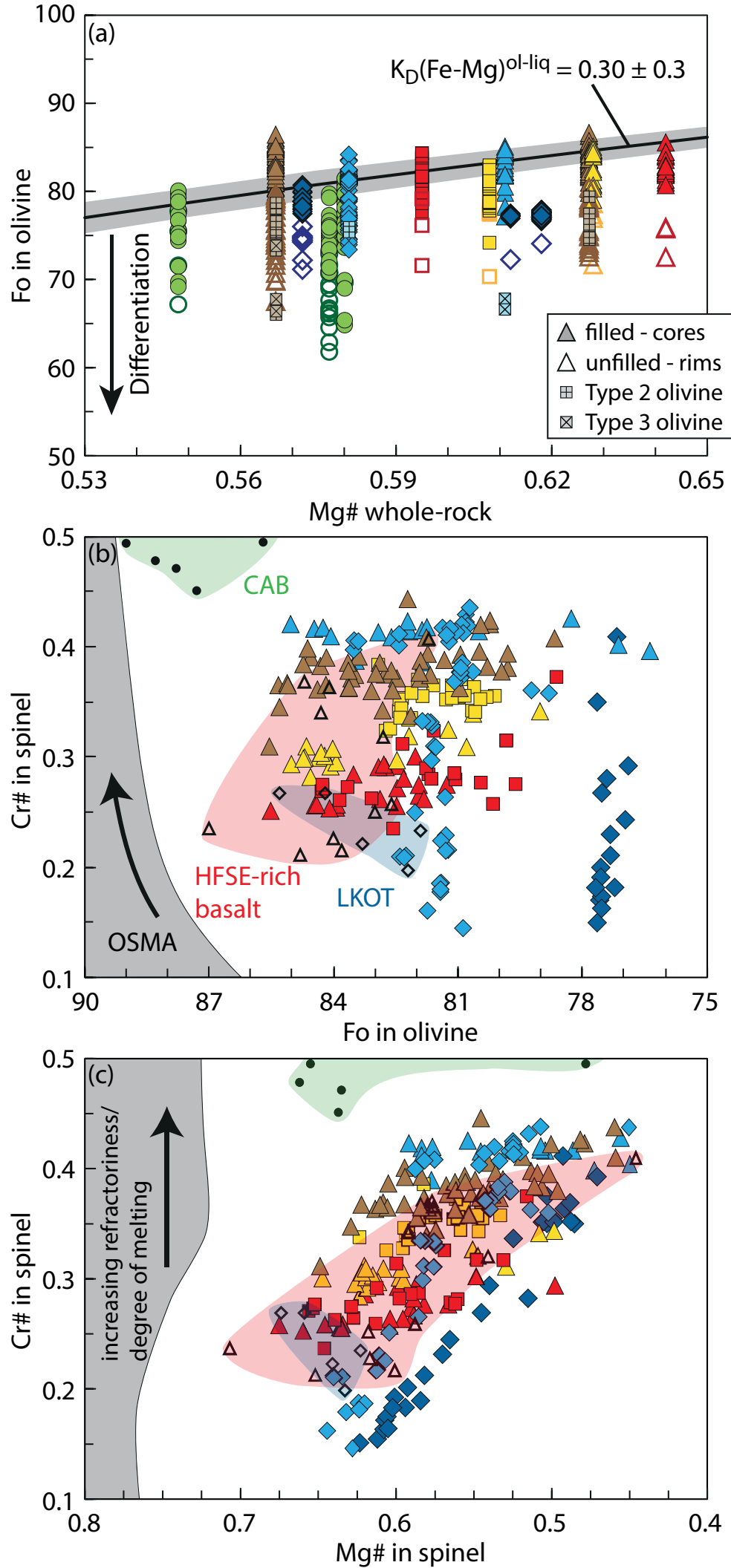


Figure 10

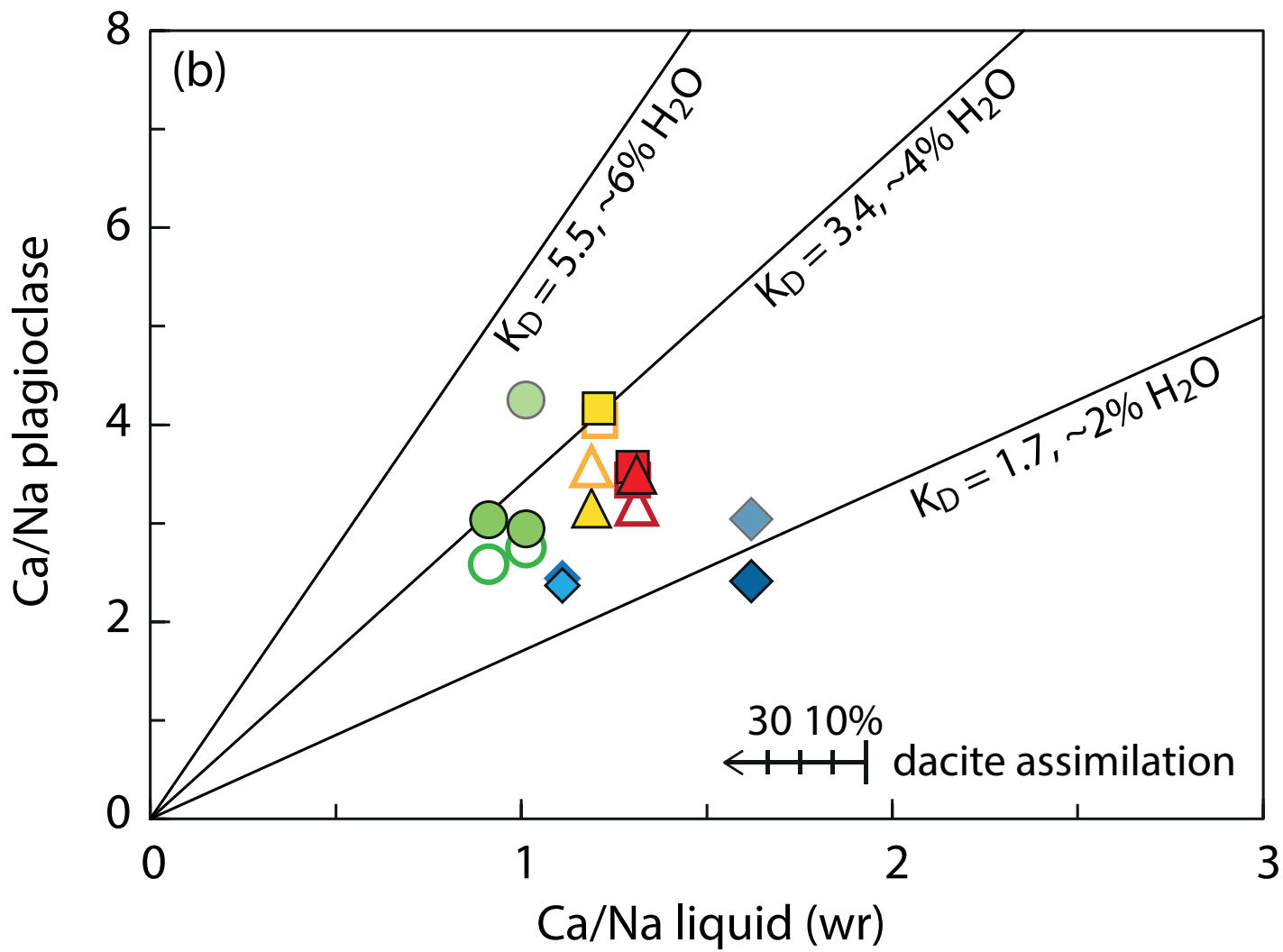
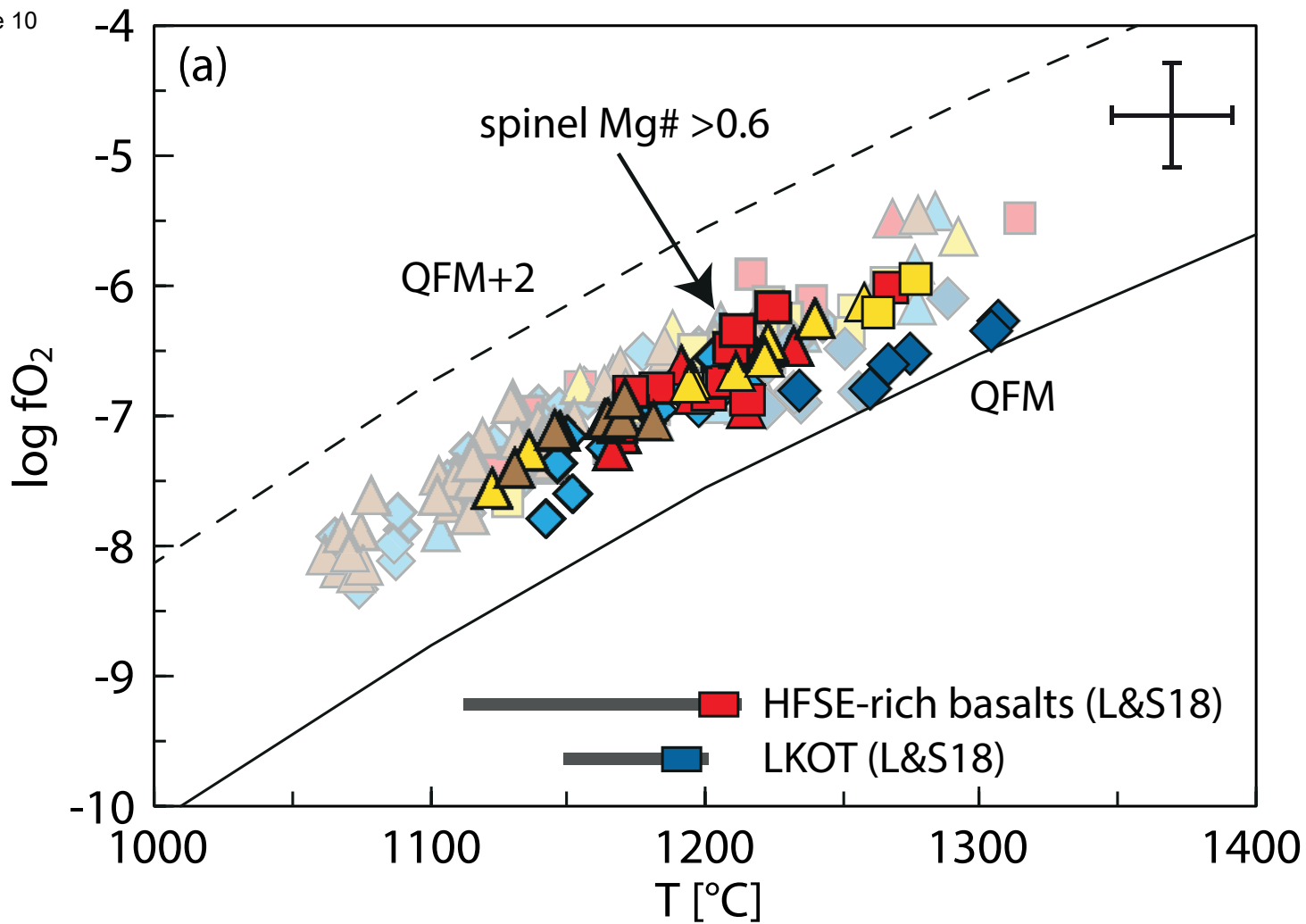


Figure 11

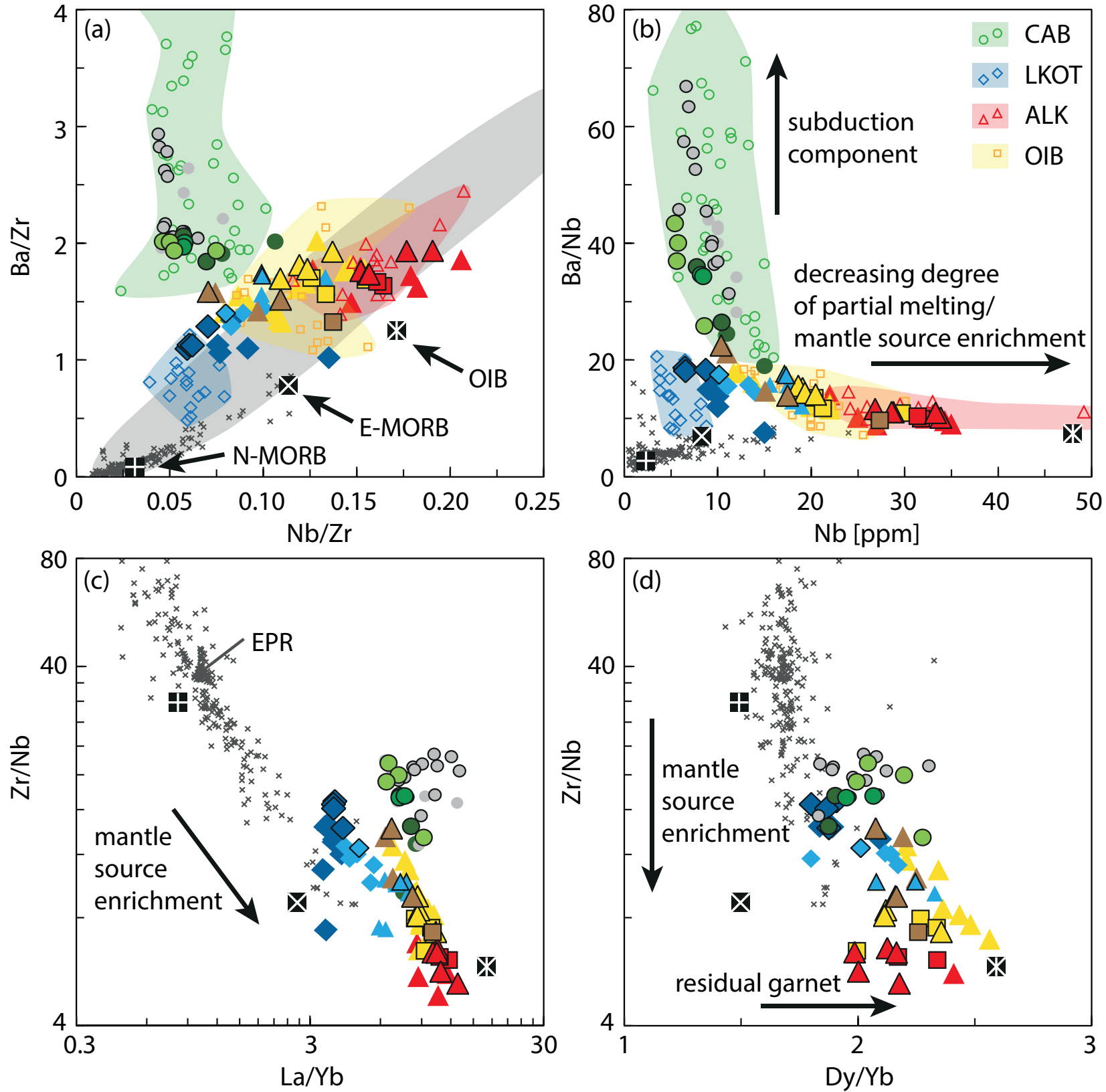


Figure 12

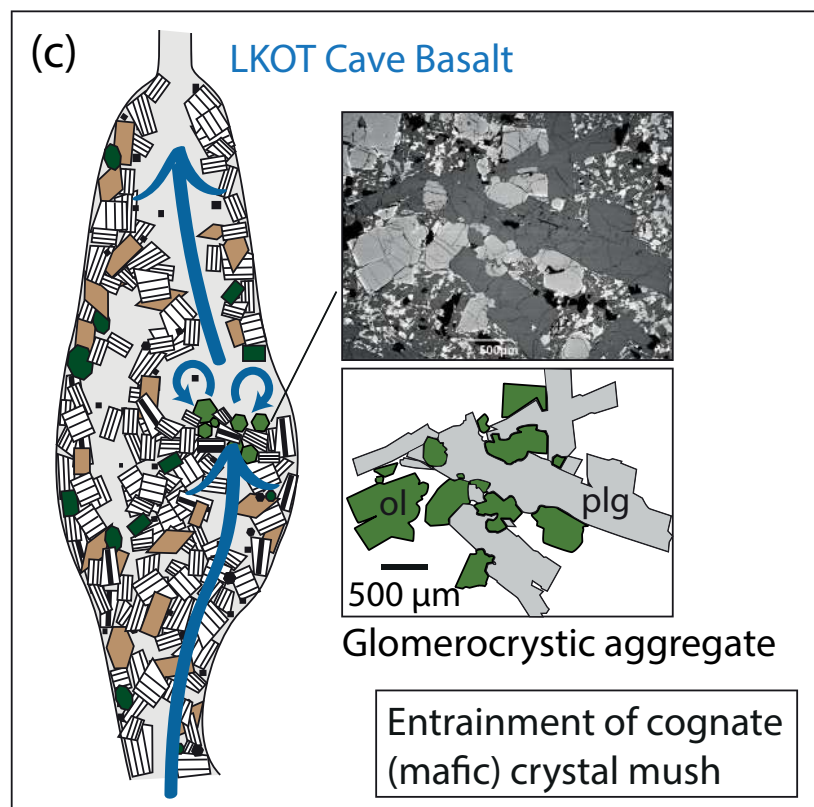
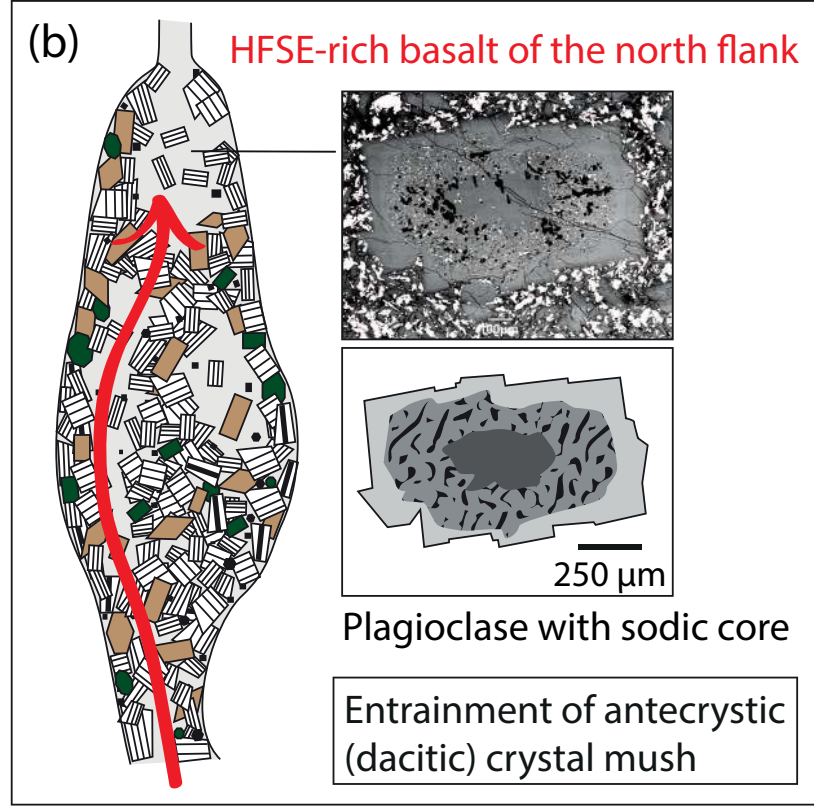
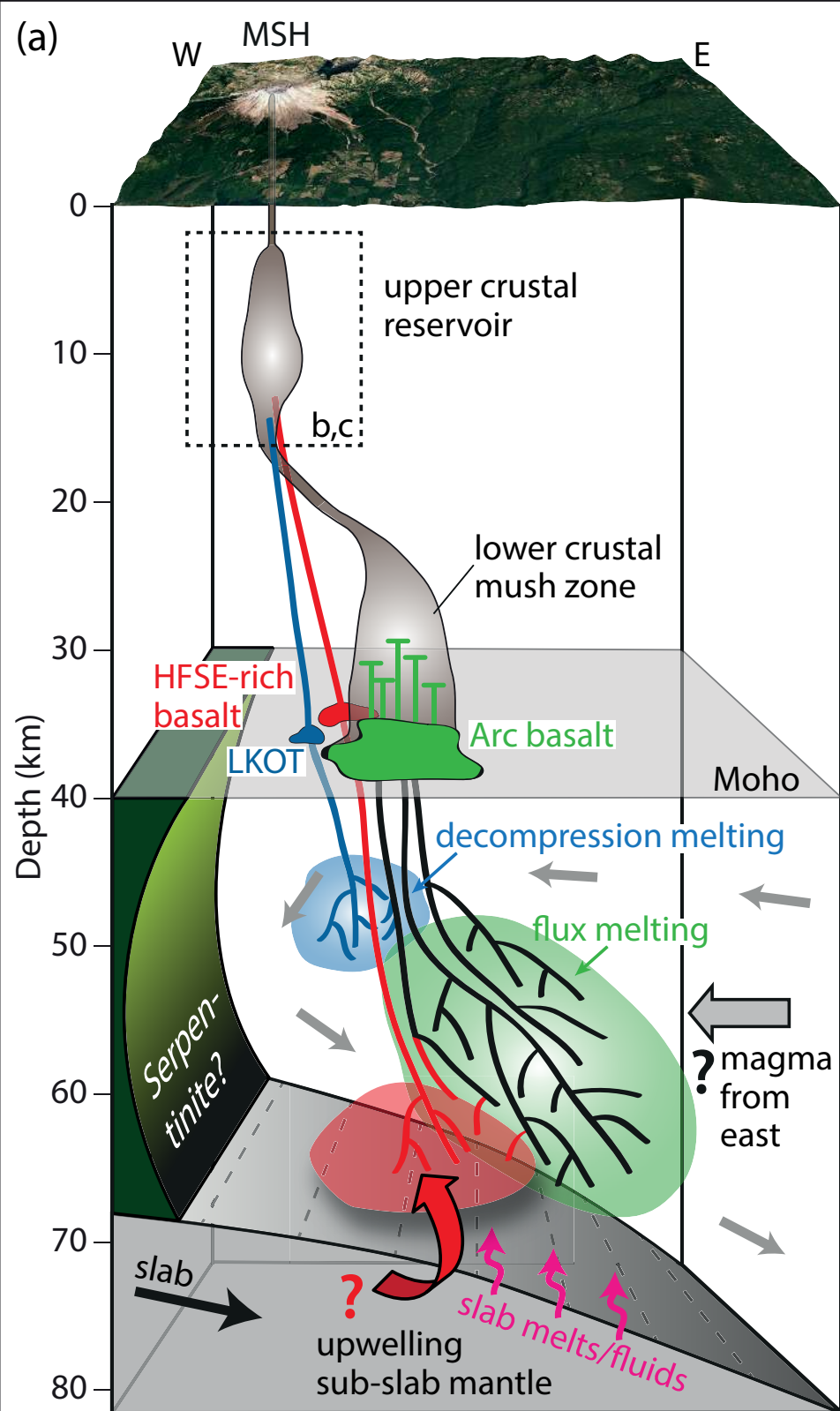





Table 1: Stratigraphy of the Castle Creek eruptive period of Mount St. Helens

Age	Symbol	Unit*	Abbr.	Rock type
<i>Late Castle Creek period (~1895-1700 years BP)</i>				
		Andesite of Loowit Trail	alt	lava flow, breccia
		Basaltic andesite of Nelson Glacier	mng	lava flows
1730±35 BP 1740±70 BP	/	Basalt of Castle Creek/Bu3 tephra	bcc/Bu3	lava flows/tephra
		Andesite of the Baguette flow (?)	ab	lava flow
		Andesite of the Plains of Abraham	apa	lava flows
1765±40 BP, 1795±30 BP		Andesite of Sasquatch Steps	ass	lava flows, lahar, pyroclastic flows
	/	Basalt of the north flank, Bu2 tephra	bnf/Bu2	lava flows/tephra
		Basaltic andesite of Truman Trail	mtt	lava flows
		Andesite of section 26	a26	lava flows
<i>Middle Castle Creek period (~1895 ± 10 BP)</i>				
1895±10 BP		Cave Basalt	bc	lava flows
	/	Pre-Cave Basalt (high-K/low-K)	bpc	lava flows
	/	Basalt of the south flank/Bu1 tephra	bsf/Bu1	lava flows/tephra
<i>Early Castle Creek period (~2025-1990 years BP)</i>				
		Dacite of Redrock Pass (?), Andesite of the North Rim, Dogs Head dome	dcc	lava flows, lava domes
		Bi tephra	Bi	tephra
1990±40 BP 2025±40 BP		Northwest dome, Dacitic lahars and pyroclastic flows	dcc	lava dome, lahars, pyroclastic flows

*Units (bcc, bpc, bsf) that encompass basaltic and basaltic andesitic compositions are referred to as basalts.

Table 2: Chemical characteristics of mafic endmembers from Mount St. Helens

Type	HFSE-rich basalt	LKOT	Arc-type basaltic andesite
Unit	(bnf, Bu2)	(bc)	(mng)
Symbol			
SiO ₂ * (wt.%)	49.4 - 50.5	49.6 - 51.1	53.9 - 56.2
MgO* (wt.%)	6.4 - 7.4	6.1 - 7.3	4.0 - 4.9
K ₂ O* (wt.%)	1.2 - 1.5	0.5 - 0.7	0.85 - 1.0
TiO ₂ * (wt.%)	1.9 - 2.2	1.4 - 1.7	1.2 - 1.4
Ni (ppm)	80 - 141	74 - 108	34 - 52
Nb (ppm)	27 - 34	6 - 9	5 - 9
Sr (ppm)	580 - 680	320 - 350	485 - 505
La/Yb	9.3 - 12.9	3.8 - 4.1	6.4 - 9.2
Dy/Yb	2.0 - 2.3	1.8 - 1.9	2.0 - 2.3
Nb/La	1.3 - 1.4	0.8	0.5 - 0.7
Ba/La	13.7 - 14.8	14.3 - 15.0	19.2 - 23.0
Olivine	≤Fo85	≤Fo81	≤Fo81
Spinel	Mg# ≤68	Mg# ≤63	Mg# ≤52
Plagioclase	≤An78	≤An75	≤An75
T (°C) [#]	1170 - 1270	1235 - 1310	
Δlog(fO ₂)QFM [#]	+0.5 to +1.1	+0.1 to +0.4	

*Range includes data from compilation in Data Repository 5

[#]T and fO₂ calculated from olivine-spinel pairs using the methods of Wan et al. (2008) and Ballhaus et al. (1990).